RESEARCH ARTICLE | OCTOBER 11 2023

Large-eddy simulation of a lean-premixed hydrogen flame in a low-swirl combustor under combustion instability

Jun Nagao (長尾順); Abhishek Lakshman Pillai; Takeshi Shoji (庄司烈); Shigeru Tachibana (立花繁); Takeshi Yokomori (横森剛); Ryoichi Kurose (黒瀬良一)

Physics of Fluids 35, 105124 (2023)
https://doi.org/10.1063/5.0166412

Physics of Fluids ARTICLE pubs.aip.org/aip/pof

Large-eddy simulation of a lean-premixed hydrogen flame in a low-swirl combustor under combustion instability

Cite as: Phys. Fluids **35**, 105124 (2023); doi: 10.1063/5.0166412
Submitted: 5 July 2023 · Accepted: 26 September 2023 ·
Published Online: 11 October 2023

View Online Export Citation CrossMark

Jun Nagao (長尾順),[1,a] Abhishek Lakshman Pillai,[1] Takeshi Shoji (庄司烈),[2] Shigeru Tachibana (立花繁),[2] Takeshi Yokomori (横森剛),[3] and Ryoichi Kurose (黒瀬良一)[1]

AFFILIATIONS

[1]Department of Mechanical Engineering and Science, Kyoto University, Kyoto daigaku-Katsura, Nishikyo-ku, Kyoto 615-8540, Japan
[2]Aviation Technology Directorate, Japan Aerospace Exploration Agency, Chofu, Tokyo 182-8522, Japan
[3]Department of Mechanical Engineering, Keio University, Yokohama, Kanagawa 223-8522, Japan

[a)]Author to whom correspondence should be addressed: nagao.jun.87c@st.kyoto-u.ac.jp

ABSTRACT

Large-eddy simulation (LES) of a lean-premixed hydrogen turbulent jet flame with combustion instability (CI) in a low-swirl combustor (LSC) is performed by employing a dynamically thickened flame model with a detailed chemical reaction model with 9 chemical species and 20 reactions, and the LES validity and the CI characteristics are investigated in detail. The results show that the present LES can accurately reproduce the experimentally observed characteristics of the CI such as intensity, frequency, sporadic decay of pressure oscillations, and a flame–flow interaction inducing the periodic transitions of an inverted conical flame structure and a flat flame structure in the LSC. The sporadic decay of pressure oscillations and the flame–flow interaction are caused by the temporal decoupling of pressure and heat release rate and the periodic outward and inward deflections of the inflow, which is associated with the flow behavior in the upstream injector channel, respectively.

I. INTRODUCTION

The development of eco-friendly gas turbine engines with high combustion efficiencies is increasingly important to solve the problem of climate change and air pollution.[1,2] Thus far, reductions in carbon dioxide (CO_2) emissions have been accomplished by increasing the compression ratio and firing temperature of gas turbine engines.[3,4] Although there are benefits to this approach, increasing the compression ratio can increase the combustion temperature and the emissions of nitrogen oxides (NO_x).[4,5] Thus, the regulations on NO_x emissions are being tightened.[6] Given this background, a method called lean-premixed combustion, in which air and fuel are well-mixed in advance and burned in a lean state to lower the combustion temperature, has gained considerable research interest as an approach to significantly reduce NO_x emissions.[7] However, lean-premixed combustion has a disadvantage in that it makes combustion unstable and enhances the probability of the occurrence of combustion instabilities.[8] Combustion instability (CI) is a type of unstable combustion which also includes flashback[9–12] or blowout,[13–15] and it is necessary to accurately predict and effectively control it before it causes large-amplitude pressure oscillations in the combustor which can lead to severe combustor damage.[16] Theoretically, it is understood that CI is provoked by the strong correlation between the pressure oscillations and heat release rate fluctuations inside a combustor.[17] However, although the basic principle of CI is clear, the detailed mechanisms of its generation and amplification are yet to be fully understood. The reasons for the incomplete understanding of CI are the complicated phenomena involved in CI and the complex geometries of actual combustors. In commercial combustors, many factors, such as the interaction of the flame with a wall surface,[18–20] fuel characteristics,[21–23] and the shape of the combustor,[24,25] affect each other.

Research works aimed at elucidating and predicting CI have been undertaken both experimentally (e.g., Refs. 26–32) and numerically (e.g., Refs. 33–39) worldwide. Among these works, an interesting experimental study of CI in lean-premixed low-swirl hydrogen turbulent jet flames was conducted recently at the Japan Aerospace Exploration Agency (JAXA).[30,31] The low-swirl flame uses a simple flame-propagation phenomenon to maintain the flame, which has the advantage of maintaining combustion without blowing off over a wide range of turbulence intensity.[40,41] Furthermore, hydrogen fuel is also attracting interest as an alternative to fossil fuels that can be used in gas turbine engines in the future because of its extremely high heating value per unit mass, and because it does not emit CO_2 when burned. Therefore, although lean-premixed low-swirl hydrogen turbulent jet flames are expected to be an effective combustion method considering the benefits mentioned above, their detailed characteristics, particularly the flame behavior under CI, are still not fully understood.

In the above-mentioned experiments[30,31] on CI in lean-premixed low-swirl hydrogen turbulent jet flames, a pattern of flame-flow dynamics, which is considered to be unique to low-swirl hydrogen turbulent jet flames, was observed for the first time. Generally, in the low-swirl combustors (LSCs), an inverted conical flame structure is commonly generated; however, under CI conditions, the flame structure of the lean-premixed hydrogen flame in the experiment[30,31] periodically switched between a wide flat flame and an inverted conical flame. These flame dynamics are accompanied by the periodic outward and inward deflections of inflow with respect to the streamwise direction. The experimental study[30,31] suggested that these periodic switching dynamics couple with the pressure oscillations, and occur in the CI. However, further simultaneous examinations using various physical quantities such as inflow velocities, pressure, gas temperature, and reaction rate in three dimensions in the whole combustor, which are very hard to be obtained only in the experiments, need to be performed to support their investigations. In addition, the information of the flow field in an upstream region is required because the periodic outward and inward deflections of the inflow are not only formed in the combustor but also affected by the phenomena in the upstream region from the region close to the swirler assembly to the injector exit.

Therefore, this study aims to elucidate the mechanism of the flame-flow dynamics of a lean-premixed hydrogen flame in an LSC under CI using large-eddy simulation (LES), which considers the swirler assembly in the upstream region. The LES employing a dynamically thickened flame model[42–47] with a detailed chemical reaction model that comprises 9 chemical species and 20 reactions[48] is performed for the same configurations of the combustor and injector as those in the experiment.[30,31] To capture and analyze the pressure oscillation phenomena in the realistic combustor and injector in the experiment,[30,31] long-term time-series data should be stored. To this end, a weakly compressible scheme,[11,35,38,49–51] which makes the LES have relatively a larger time increment, is used here.

II. NUMERICAL METHODS

A. Governing equations

The governing equations used in this LES employing a dynamically thickened flame model[42–47] are the Favre-filtered form of the conservation equations of mass, momentum, enthalpy, and mass fraction of chemical species, along with the equation of state for ideal gas, and they are expressed as follows:

$$\frac{\partial \bar{\rho}}{\partial t} + \nabla \cdot (\bar{\rho}\tilde{\boldsymbol{u}}) = 0, \tag{1}$$

$$\frac{\partial \bar{\rho}\tilde{\boldsymbol{u}}}{\partial t} + \nabla \cdot (\bar{\rho}\tilde{\boldsymbol{u}}\tilde{\boldsymbol{u}}) = -\nabla \bar{P} + \nabla \cdot \bar{\boldsymbol{\sigma}}, \tag{2}$$

$$\frac{\partial \bar{\rho}\tilde{h}}{\partial t} + \nabla \cdot (\bar{\rho}\tilde{h}\tilde{\boldsymbol{u}}) = \frac{D\bar{P}}{Dt} + \nabla \cdot \left[\bar{\rho}\left\{EFD_h + (1-\Omega)D_t\right\}\nabla\tilde{h}\right] + \nabla \cdot \left[\bar{\rho}EF\left\{\sum_k \tilde{h_k}(D_k - D_h)\nabla\tilde{Y}_k\right\}\right] + \bar{\boldsymbol{\sigma}} : \nabla\tilde{\boldsymbol{u}}, \tag{3}$$

$$\frac{\partial \bar{\rho}\tilde{Y}_k}{\partial t} + \nabla \cdot (\bar{\rho}\tilde{Y}_k\tilde{\boldsymbol{u}}) = \nabla \cdot \left[\bar{\rho}\left\{EFD_k + (1-\Omega)D_t\right\}\nabla\tilde{Y}_k\right] + \frac{E}{F}S_{comb,k}, \tag{4}$$

$$\bar{P} = \bar{\rho}R\tilde{T}. \tag{5}$$

Here, the overbar $^{-}$ denotes the spatially filtered mean value of the physical quantity in grid scale for LES, and the tilde $\tilde{}$ denotes the Favre-averaged value. ρ, $\boldsymbol{u}$, h, and Y_k are the density, velocity, gas mixture specific enthalpy, and mass fraction of species k, respectively. P, h_k, R, and T are pressure, specific enthalpy of species k, gas constant, and temperature, respectively. $\boldsymbol{\sigma}$ is the stress tensor which includes both the resolved and the subgrid scale (SGS) stress. D_h, D_k, and D_t are the thermal diffusivity, mass diffusion coefficient of species k, and turbulence diffusion coefficient, respectively. Here, D_h is expressed as $\rho D_h = \lambda / c_p$, where λ is the heat conductivity and c_p is the specific heat capacity. D_k is calculated from the equation: $\boldsymbol{V_k} Y_k = -D_k \nabla Y_k$, where $\boldsymbol{V_k}$ is the diffusion velocity of species k, and the diffusion velocities of the different species are evaluated by solving the system of linear equations.[52,53] The binary diffusion coefficients required for diffusion calculation are obtained from CHEMKIN.[54] The SGS terms are calculated using the dynamic Smagorinsky model.[55,56] The consumption or production rate of species k is represented by the term $S_{comb,k}$. In this study, hydrogen combustion is modeled using a detailed chemical reaction model proposed by Miller and Bowman, which comprises 9 chemical species and 20 reactions,[48] and shows favorable agreement with measurements of the laminar flame speed, especially at lower equivalence ratios, as depicted in Fig. 1 of Ref. 57. Ω is the flame sensor,[42,45,46] which is used to detect the flame front position, and varies from zero in the fully burned or unburned regions to unity in the reaction zone, and it is defined as

$$\Omega = \tanh\left(\alpha \frac{q}{q_{max}}\right). \tag{6}$$

Here, q is the local heat release rate, and q_{max} is the maximum heat release rate derived from the calculation of one-dimensional laminar flame. α is the parameter controlling the thickness of the transition layer between thickened and non-thickened zones, and its value in the gas combustion system is defined as $\alpha = 10$ based on the previous study.[35] F is a thickening factor used to thicken the flame, in order to resolve the flame with at least five LES grid points, and E is an efficiency function that accounts for the loss of flame wrinkling owing to artificial thickening of the flame. The thickening factor is calculated as

$$F = (F_{max} - 1)\Omega + 1, \tag{7}$$

and the maximum value, F_{max} is estimated using

$$F_{\max} = \max\left(\frac{n\Delta_{\text{mesh}}}{\delta_l^0}, 1\right). \tag{8}$$

Here, Δ_{mesh} is the cell size, δ_l^0 is the laminar flame thickness, and n is the parameter to control the grid points inside flame thickness, which

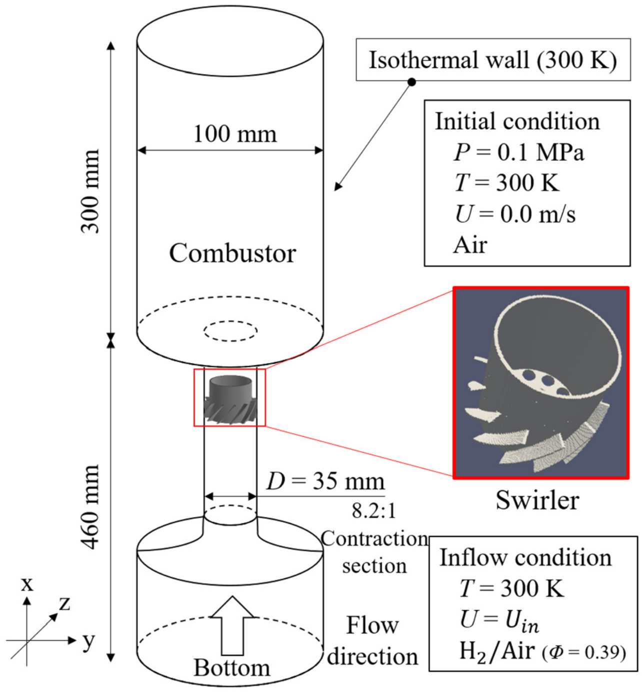

FIG. 1. Schematic of the computational domain and conditions.

is set to 5 based on the previous study.[43,45] The calculation method of the efficiency function is intricate, so refer to Refs. 42–47.

B. Computational setup

LES is performed for a LSC. A schematic of the computational domain and conditions for the combustor system is shown in Fig. 1, and the entire computational domain and grid distribution are illustrated in Fig. 2. The configuration of the combustor is set to recreate the experimental setup employed by Shoji *et al.*[30,31] The system has a combustor and an injector. The diameter and length of the combustor are 100 and 300 mm, respectively. The injector consists of an 8.2:1 area-ratio contraction section, and the diameter of the injector that contains the swirler assembly is 35 mm. The length of the entire injector is 460 mm. The swirler, whose swirl number is 0.39, is placed approximately 43 mm upstream of the injector exit. The components of the swirler are 12 curved vanes inclined at 37° to the combustor axis, a perforated plate, and a central tube. Additional details of the entire combustor system are available in Refs. 30 and 31. The computational domain is discretized using a non-uniform staggered Cartesian grid, with fine grid-spacing around the swirler, main combustion region, and walls. Initially, the entire region is filled with stationary air at a pressure of 0.1 MPa and a temperature of 300 K. As inflow conditions, the completely premixed gas of air and fuel (hydrogen) is introduced into the combustor system from the bottom. The temperature of the premixed gas is 300 K, and the equivalence ratio is 0.39. The inflow velocity is set to maintain a constant incoming mass flow rate of the premixed gas and is derived as follows. First, the conservation of the mass flow rate is expressed as:

$$\rho_{in} A_{bottom} U_{in} = \rho_0 A_{bottom} U_0. \tag{9}$$

Here, ρ is the density of premixed gas, A_{bottom} is the inlet area at the bottom of the system from where the premixed gas is introduced, and U is the inflow velocity. Subscripts 0 and *in* represent the inflow conditions at $t = 0$ s (i.e., initial condition) and at each time step for $t > 0$ s, respectively. The above equation can be rewritten using the equation of state for ideal gas, and the inflow velocity is expressed as

$$U_{in} = \frac{P_0 T_{in}}{P_{in} T_0} U_0. \tag{10}$$

The initial inflow velocity, U_0, is set in accordance with the experimental premixed gas mass flow rate, such that the bulk mixture velocity at

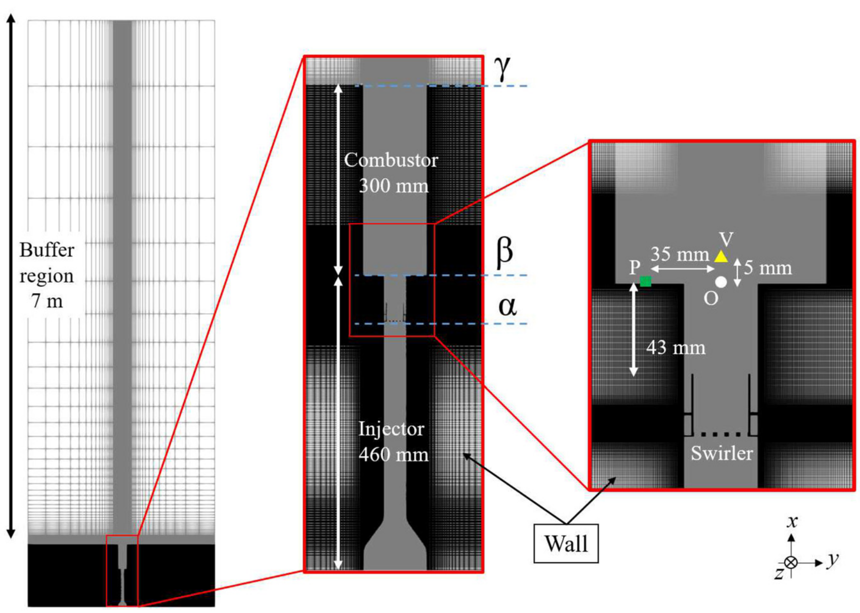

FIG. 2. Computational grid of LES.

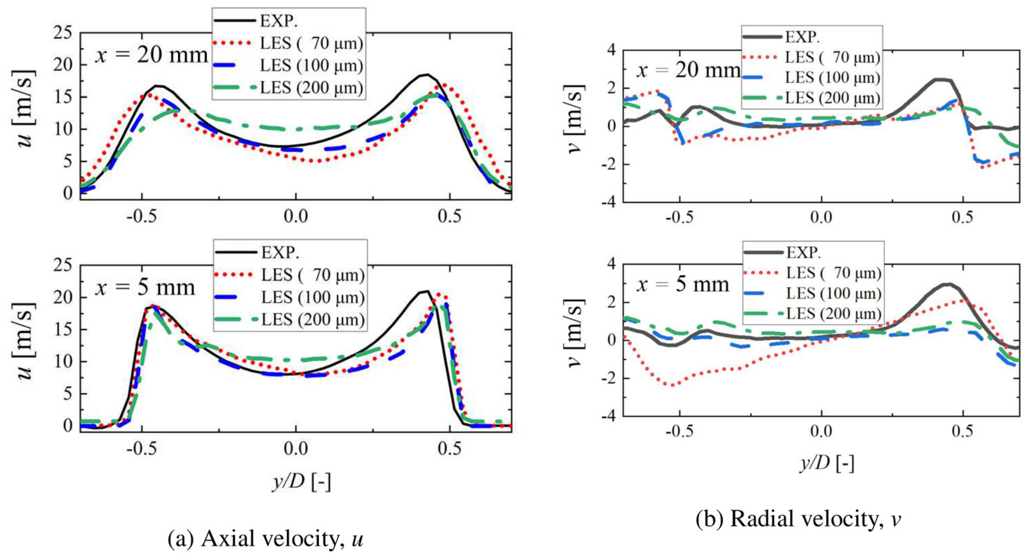

FIG. 3. Comparison of the time-averaged (a) axial and (b) radial velocity between the experimental data and LES predictions using three different grid spacings (70, 100, and 200 μm) for an open configuration without reactions.

the injector exit is 15 m/s.[30,31] To consider the interaction between the walls and the fluid, no-slip boundary conditions are applied on the wall surfaces, and the wall temperature is maintained at 300 K by adopting an isothermal wall condition. The x-axis points in the streamwise direction, and the y- and z-axes are orthogonal to the x-axis and each other. The origin of the coordinate sits at the center of the injector-exit plane (as represented by a white point, O, in Fig. 2). In addition to the injector and combustor region, the grid consists of a buffer region to damp the spurious reflections at the outflow and lateral boundaries, which was confirmed essential settings for the simulation of CI to be accurately predicted in the previous study.[34]

The reliability of the grid resolution is confirmed by comparing the LES results obtained with three different minimum grid spacings (70, 100, and 200 μm) with the experimental results for an open configuration (i.e., the system without the combustor wall but with the same injector section) without reactions. The experimental measurements of the open configuration flow without reactions (i.e., cold flow) were conducted at JAXA, and the cold flow LESs using the aforementioned three different minimum grid spacings were performed for the same conditions as those in the experiment. These conditions for the bulk mixture velocity and ambient pressure and temperature of the cold flow are the same as those mentioned above. The radial distributions of time-averaged axial and radial velocity at $x = 5$ and $x = 20$ mm are shown in Fig. 3. Figure 3(a) shows that the time-averaged radial distributions of axial velocity calculated using 70 and 100 μm grid spacings are in an overall favorable agreement with the experimental results, albeit with some minor errors. In contrast, the results calculated using the 200 μm grid spacing have larger velocity errors, particularly around the combustor axis (i.e., $y/D = 0$) at $x = 5$ mm, and the discrepancy is larger at $x = 20$ mm across all radial positions. Furthermore, Fig. 3(b) indicates that, at the upstream position of $x = 5$ mm, the time-averaged radial distribution of radial velocity calculated using 70 μm grid spacing agrees with the experimental results better than results with the other grid spacings. Moreover, around the streamwise position of $x = 20$ mm, where the fuel undergoes combustion in the LES of CI, the results with 70 and 100 μm grid spacings show almost similar trends in the distributions in contrast to that with 200 μm. Moreover, the absolute errors from the experiment at the peak values are listed in Table I. Based on the above considerations, a minimum grid spacing of 100 μm is adopted for the region around the swirler and combustion region of the LES of CI in this study.

The pressure and velocity variations used in the following discussion are sampled at the point 35 mm away from the origin in the radial direction (as represented by the green square, P, in Fig. 2) and the point 5 mm away from the origin in the axial direction (as represented by the yellow triangle, V, in Fig. 2), respectively, which are the same positions used in the experiment.[30,31] The LES is performed using an in-house code FK^3 (Ref. 58) that can capture the pressure perturbations by employing a pressure-based semi-implicit algorithm for compressible flows.[49] The KK scheme[59] is employed to calculate the convection term of the momentum equation, and the WENO scheme[60] is used to evaluate the convection terms in the scalar transport equations. The third-order explicit total variation diminishing (TVD) Runge–Kutta method is used for time advancement. The thermophysical properties and transport coefficient are acquired from CHEMKIN.[54] The LES domain is discretized using 614.4×10^6 grid

TABLE I. Absolute error of peak values of the velocity distribution of cold flow.

Grid size (μm)	u (at $x = 5$ mm) (m/s)	u (at $x = 20$ mm) (m/s)	v (at $x = 5$ mm) (m/s)	v (at $x = 20$ mm) (m/s)
70	0.49	1.62	0.87	1.19
100	1.35	3.05	2.36	1.00
200	1.70	3.24	1.95	1.46

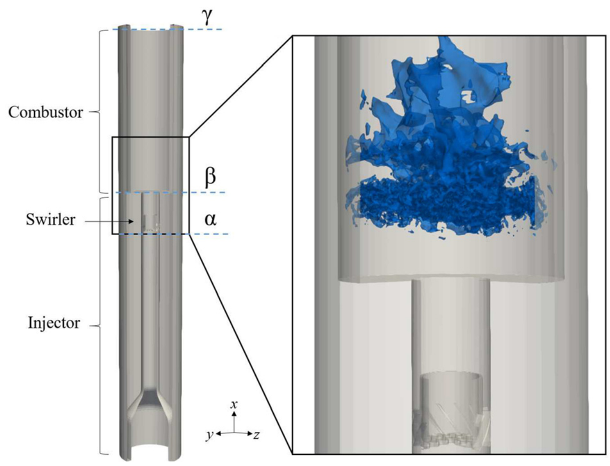

FIG. 4. Instantaneous 3D distribution of the isosurface of temperature at 1400 K (colored in blue) in the LSC obtained from the LES.

points (1500 grid points in the x-direction × 640 grid points in the y-direction × 640 grid points in the z-direction). In this LES, the time interval of approximately 0.25 s is simulated to acquire statistic data, and the computational time is about 260 h by parallel computation using 61 440 cores on the supercomputer Fugaku provided by the RIKEN Center for Computational Science.

III. RESULTS AND DISCUSSION

A. Characteristics of combustion instability

This section provides an overview of the flame and the flow field and validates this LES by comparing oscillation characteristics.

Figure 4 shows the flame obtained from the LES represented by an isosurface of temperature at 1400 K in the LSC, which is colored in blue. The temperature isosurface is not distributed in the vicinity of the injector exit, which gives rise to forms of a lifted flame. Also, in the experiment, a lifted flame was observed, which means that this LES reproduces the basic flame characteristics well. In the outer recirculation zone (ORZ), the temperature of the burnt gas decreases because of the heat loss on the wall surface when the gas flows from downstream to upstream under the influence of the recirculating flow, as depicted in Fig. 5(a) which shows the instantaneous distribution of the temperature on the x–y plane obtained from the LES. Thus, coupled with the condition of the balance between the turbulent flame speed and inflow velocity, a lifted flame is formed by the relatively low temperature of the burnt gas near the injector exit in contact with the unburnt gas. Moreover, Fig. 5(b) shows the instantaneous distribution of the mass fraction of OH (Y_{OH}) on the x–y plane obtained from the LES, which allows us to observe the combustion characteristics of the lean-premixed hydrogen flame at the flame front. The shape of the lean-premixed hydrogen flame front is more complex than that of hydrocarbon fuels such as methane because of the strong effect of preferential diffusion. For the lean-premixed hydrogen flame, it has been experimentally and numerically confirmed that the convex flame fronts (i.e., with positive curvatures) are more reactive regions, and the concave flame fronts (i.e., with negative curvatures) are less reactive regions.[61] The Y_{OH} distribution obtained from the LES shows that the flame has a highly complex cellular structure, and combustion occurs more actively on the convex flame front owing to the effect of preferential diffusion.

To explore the effect of preferential diffusion in a more quantitative way, Fig. 6 shows the joint probability density function, Joint PDF, of flame surface curvature vs mass fraction of OH, Y_{OH} obtained from the LES, on the isosurface of temperature at 1000 K which is almost the same temperature used in Ref. 61. Here, the curvature, κ, is defined as $\kappa = \nabla \cdot n$ where $n = -\nabla T/|\nabla T|$, and the positive normal vectors, n point toward the unburnt gas side from downstream. Similar to the previous studies that report the effect of preferential diffusion,[61–63] the correlation of the curvature and the Y_{OH} has a positive correlation, and as mentioned above, Y_{OH} is higher at positive curvatures and lower at negative curvatures.

To compare the oscillation characteristics, Fig. 7 shows the time variation of pressure measured at point P (green square symbol in Fig. 2) obtained from the LES along with the experimental results.

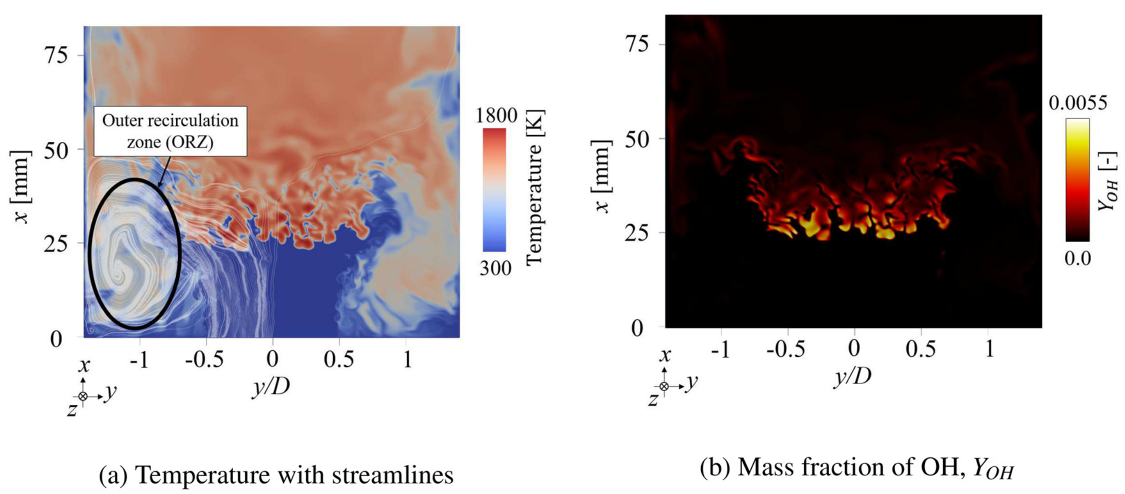

FIG. 5. Instantaneous distribution of (a) temperature and (b) mass fraction of OH on the x–y plane (z = 0 mm) obtained from the LES.

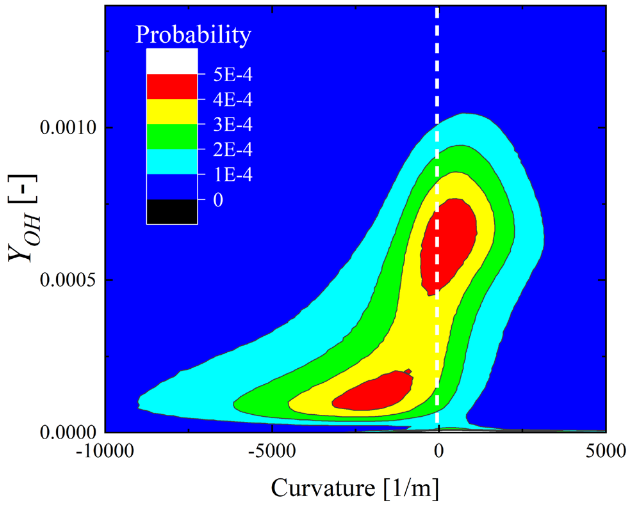

FIG. 6. Distribution of Joint PDF of curvature vs mass fraction of OH, Y_{OH} obtained from the LES, on the isosurface of temperature at 1000 K (preferential diffusion effect).

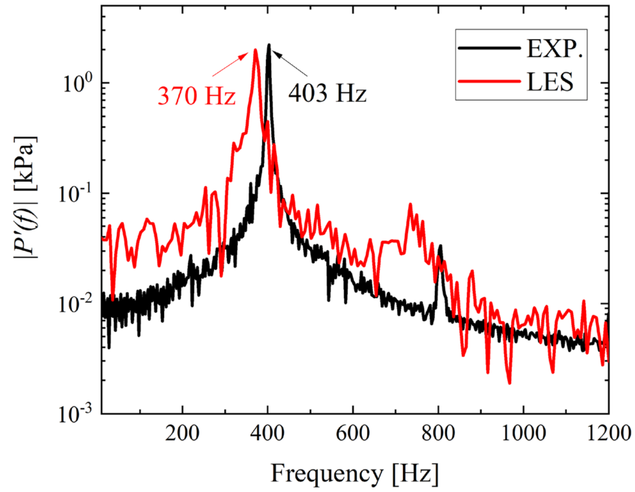

FIG. 8. Comparison of the power spectra of pressure oscillations between experimental data[30,31] and LES prediction.

The pressure oscillates strongly with a maximum amplitude of about 4 kPa. During CI, pressure oscillations are sporadically weakened a few times as indicated by the black arrows in both the LES and the experiment; however, it does not get fully damped and regains a higher amplitude after a certain period. The underlying mechanisms which cause this phenomenon are described in detail in Sec. III D. Moreover, to confirm the quantitative reproduction accuracy of the pressure oscillations, Fig. 8 shows a comparison of the power spectra of the pressure oscillations between the experiment[30,31] and LES. The peak frequency of the pressure oscillations is 403 Hz in the experiment, while it is 370 Hz in the LES. There is a minor gap of approximately 30 Hz between the experimental result and the LES's result, and this is because of the unavoidable differences between the LES and reality, such as the reproducibility of the complicated wall temperature distribution and complex swirler shape in the LES. In addition, the peak frequency varied in the same order day-by-day depending on the atmospheric conditions even in the experiment. The amplitude at the peak of the oscillations is almost 2 kPa in both the experiment and the LES with approximately 10% error between them, and it indicates that the present simulation can accurately reproduce not only the frequency but also the amplitude of the pressure oscillations.

These pressure oscillations occur in response to the heat release rate fluctuations, so acoustic flame response analysis using the acoustic flame transfer function is conducted here, which is able to describe the response sensitivity of pressure oscillation from heat release rate fluctuations. This analysis is mostly used for the open flame without combustion instability, but in this study, these responses under the influence of resonant pressure oscillation are examined for comparison with other literature. The detailed procedures of calculating the acoustic flame transfer function follow the previous literature.[64] Here, the pressure is measured at point P (green square symbol in Fig. 2), and the heat release rate is the total value inside the combustor obtained from the LES. Figure 9 shows the acoustic flame transfer function, F_{pq}, vs flame Strouhal number, St. At the lower St, the value of F_{pq} is low,

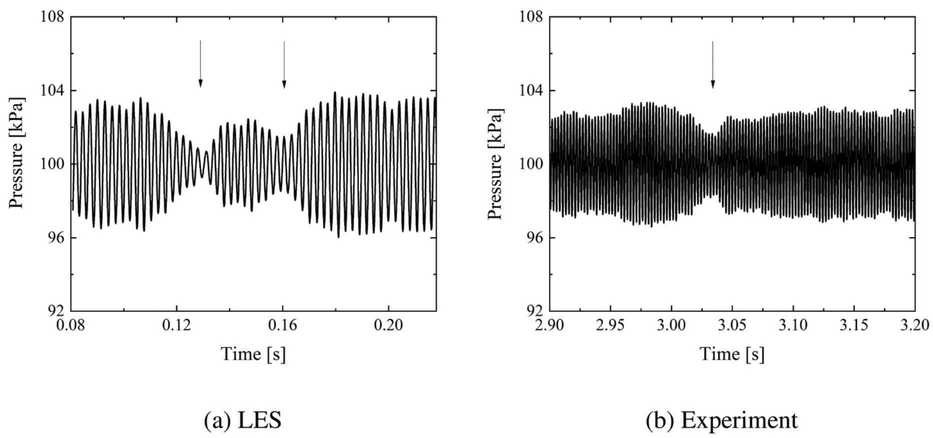

FIG. 7. Time series of pressure at point P (green square symbol in Fig. 2) in the combustor during CI from (a) LES and (b) experiment.

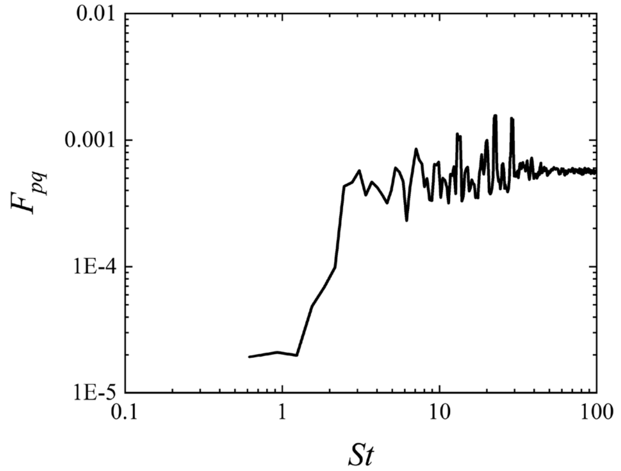

FIG. 9. Acoustic flame transfer function F_{pq} vs flame Strouhal number, $St = L_f/u_0$, where is wave number, L_f is mean flame height, and u_0 is time averaged axial velocity using the data obtained from the LES.

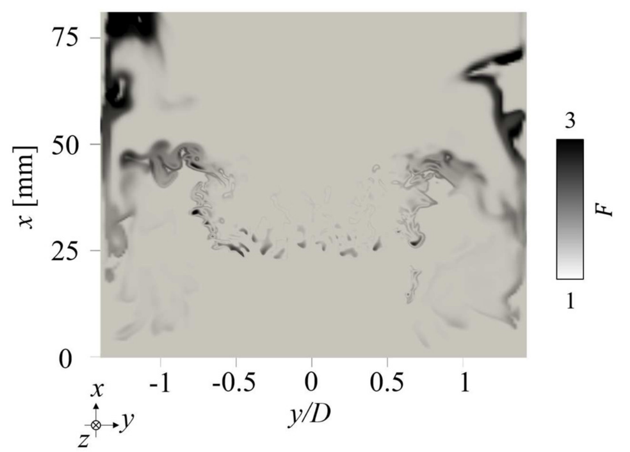

FIG. 10. Instantaneous distribution of thickening factor, F, on the x–y plane ($z = 0$ mm) obtained from the LES.

and at $St > 3$ (St ≈ 4 corresponds to resonant mode frequency of $f = 370$ Hz), it has a high plateau distribution. This distribution is qualitatively similar to those of the open jet flames investigated by Rajaram and Lieuwen[65] and Schlimpert *et al.*[64] and means that the pressure oscillation does not respond to the heat release rate fluctuation at the lower St conditions, but it responds at $St > 3$. However, at higher St conditions, the amplitude of heat release rate fluctuation was found to be almost negligible compared with that at the resonant mode. Therefore, the higher F_{pq} at higher St does not mean that the flame response at higher St has an eminent impact on combustion instability.

Here, concerning the use of the dynamically thickened flame model, the effect of flame thickening on the correlation of flame and pressure could be non-negligible. For instance, another study[66] investigated the effect of flame thickening on combustion. In particular, since that study targeted combustion noise and the turbulence structure near the flame surface significantly affect noise characteristics, it was essential to investigate the effect of flame thickening. However, this LES studies combustion instability in which a larger vortex has more dominant effects. Moreover, this LES is conducted with a relatively fine computational grid for the lean hydrogen flame. Figure 10 shows the instantaneous distribution of the thickening factor, F, on the x–y plane ($z = 0$ mm) obtained from the LES. As this figure shows, the maximum value of F is less than 3, which is small compared with 5–30 in the previous study.[47] Therefore, the effect of the thickening factor F is expected not to significantly affect the results.

Also, to examine the oscillations of other physical quantities along with the pressure in the combustor during CI in more detail, the time variations of pressure, velocity, global heat release rate, and normalized axial-stretch rate of axial velocity, $a_u = (du/dx)/U_0$, are shown in Fig. 11. The velocity shown in this figure is the value at point V (yellow triangular symbol in Fig. 2), the heat release rate is the total value inside the combustor, and the stretch rate is calculated with the data of the axial velocity, u, with a length of approximately 5 mm near the injector exit. In order to compare this LES results with the experimental results, Fig. 11 also shows the phase-averaged fluctuations of pressure, velocity, global OH* chemiluminescence intensity which provide information of heat release rate,[67,68] and normalized axial-stretch rate of axial velocity. Here, the heat release rate is not available in the experiment, and therefore, the heat release rate fluctuation in the LES

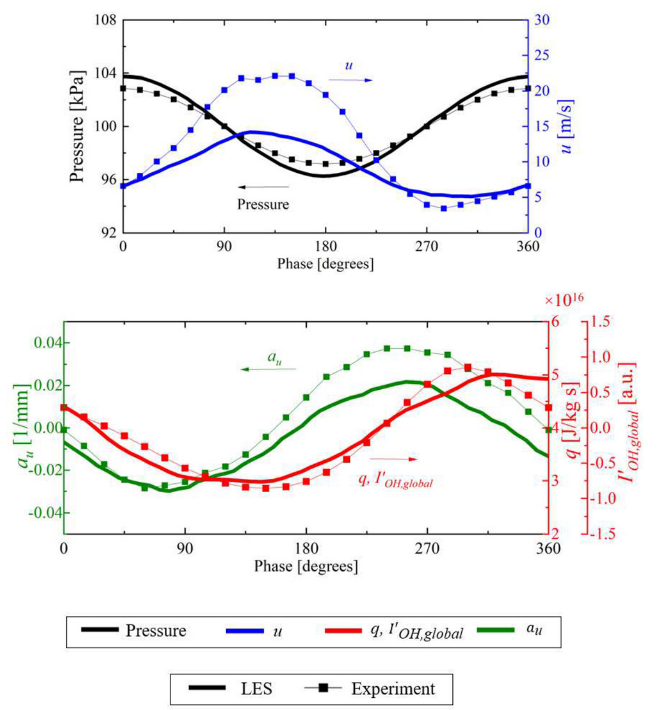

FIG. 11. Comparison of the instantaneous fluctuations in LES and the phase-averaged fluctuations in Experiment of pressure at point P (green square symbol in Fig. 2), axial velocity, u, at point V (yellow triangular symbol in Fig. 2), total heat release rate, q which is substituted for global OH$*$ chemiluminescence intensity, $I_{OH}, global$ in the experiment, and normalized axial-stretch rate of axial velocity, a_u, near the injector exit in the combustor.

is compared with the OH$*$ chemiluminescence intensity fluctuation in the experiment. The pressure and velocity oscillate at the same frequency; however, they have a phase difference of about 90°, which is the same as the phase difference observed in the experiment. In addition to the pressure-velocity phase difference, the phase differences between pressure, heat release rate (the OH$*$ chemiluminescence intensity in the experiment), and stretch rate in the LES are almost the same as those in the experiment. Moreover, the stretch rate fluctuates and attains both positive and negative values even though the value remains negative in low-swirl flow with steady conditions. This trend of the stretch rate fluctuation is also confirmed in the experimental study, and it demonstrates the reproduction of the diverging and converging flow fluctuations. Moreover, the phase difference of the axial velocity and stretch rate from pressure is also similar to those reported in a previous study of combustion instability in a similar low-swirl combustor.[69] However, in that study,[69] the stretch rate oscillates in the negative range, whereas in the present combustion instability, the stretch rate oscillates, ranging from positive to negative values. Some quantitative difference exists in terms of the peak-to-zero amplitude, such that the LES's result of the velocity fluctuation, $|u'| \approx 5$ m/s, is smaller than that of the experiment, $|u'| \approx 8$ m/s, and the LES's result of the stretch rate fluctuation, $|a'_u| \approx 0.03\,\text{mm}^{-1}$, is smaller than that of the experiment, $|a'_u| \approx 0.04\text{mm}^{-1}$. The difference in the velocity fluctuation from the experiment is considered to be primarily due to the discrepancy in the pressure gradient fluctuation in the inlet channel of LES from the experiment.

To summarize this section, the combustion instability predicted by the LES is validated by comparing the pressure oscillation and fluctuations of velocity, heat release rate, and stretch rate of axial velocity with the experimental results. In addition, the fundamental flame characteristics, such as lifted flame and preferential diffusion effect, are confirmed, and sporadic decay of pressure, which also emerges in the experiment, is observed in this LES study.

B. Flame-flow dynamics

In this section, the correlation of pressure oscillation and heat release rate fluctuation is investigated, and it is discussed with flame and flow fluctuations.

Figure 12 shows the local Rayleigh Index (*RI*) distribution on the *x*–*y* plane calculated from the LES data. This local *RI* is expressed by the following equation:

$$RI = \frac{1}{t_s}\int \frac{P'q'}{P_{ave}q_{ave}}\,dt. \tag{11}$$

Here, P' and q' represent the fluctuations in pressure, P, and heat release rate, q, respectively. P_{ave} and q_{ave} represent the time-averaged values, and t_s represents the sampling time. This index is used to visualize the regions of space in which the pressure oscillations and heat release rate fluctuations are highly correlated. The high positive local *RI* is found to be mainly distributed in regions denoted by $20\,\text{mm} < x < 50\,\text{mm}$ and $0.4 < |y/D| < 1.3$ (circled in white in Fig. 12), and no significant positive or negative correlation is observed in the other regions. The same distribution of correlation mode was also obtained using the dynamic mode decomposition (DMD) analysis. To explain this local *RI* distribution and to discuss flame fluctuation behaviors, Fig. 13 shows the phase-averaged values of Y_{OH} on the *x*–*y* plane at

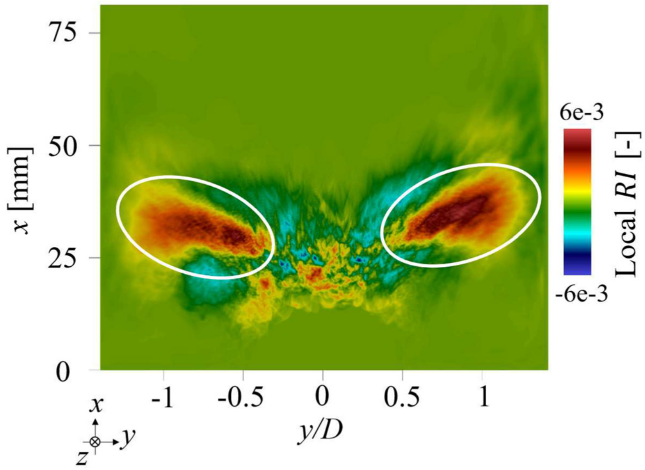

FIG. 12. Distribution of local Rayleigh Index, *RI*, on the $x-y$ plane ($z = 0$ mm) calculated from the LES data.

various phases $(\theta = 0°, 45°, 90°, 135°, 180°, 225°, 270°, 315°)$ obtained from the LES in comparison with experimental results. These experimental figures of Abel-deconvoluted OH$*$ chemiluminescence were adapted from Ref. 30. The Y_{OH} distribution shows that the flame has an inverted conical shape around the phase $\theta = 0°$; this is a typical flame structure of stable low-swirl flames. However, the flame structure transitions as the phase progresses, and around the phase $\theta = 180°$, the flame structure is flat in the upstream part of the flame at $x \approx 25\,\text{mm}$ and $|y/D| < 0.5$. Then, the flame structure returns to an inverted conical shape as the phase advances further, and this change in the flame structure is repeated periodically. The periodic fluctuation between the inverted conical flame and the flat flame was also observed experimentally,[30,31] but this periodic transition of flame structure was not observed in the other paper which also targeted the combustion instability in the low-swirl combustor.[69] At the phase $\theta = 0°$, when the pressure is maximum, the flame propagates radially toward the combustor's lateral wall, and the heat release rate becomes high in the region surrounded by the green dotted line shown in Fig. 13, and as mentioned above, the local *RI* exhibits high positive values in the same regions. In summary, since the velocity fluctuations do not perfectly match the experimental result, the flame fluctuations are also weaker than in the experiment. However, similar fluctuation phenomena are observed such as the appearance of inverted conical flames and flat flames.

Such transitions in the flame structure are attributed to changes in the velocity field inside the combustor. Therefore, Fig. 14 shows the phase-averaged velocity magnitude distribution on the *x*–*y* plane for each phase obtained from the LES. Under steady operating conditions (i.e., without CI), the low-swirl inflow spreads radially outward with respect to the streamwise direction. However, under CI, the direction of inflow inside the combustor can deflect radially inward in the region $0\,\text{mm} < x < 25\,\text{mm}$ around the phase $\theta = 270°$, and the inflow velocity is slower than the other phases. As the phase advances toward $\theta = 90°$, a fast flow directed radially outward with respect to the streamwise direction is introduced into the combustor from the injector. Thereafter, the flow velocity distribution transitions to a slow and inward-deflected flow again. This is a switching phenomenon of low-swirl flow under strong CI conditions, which was also observed in

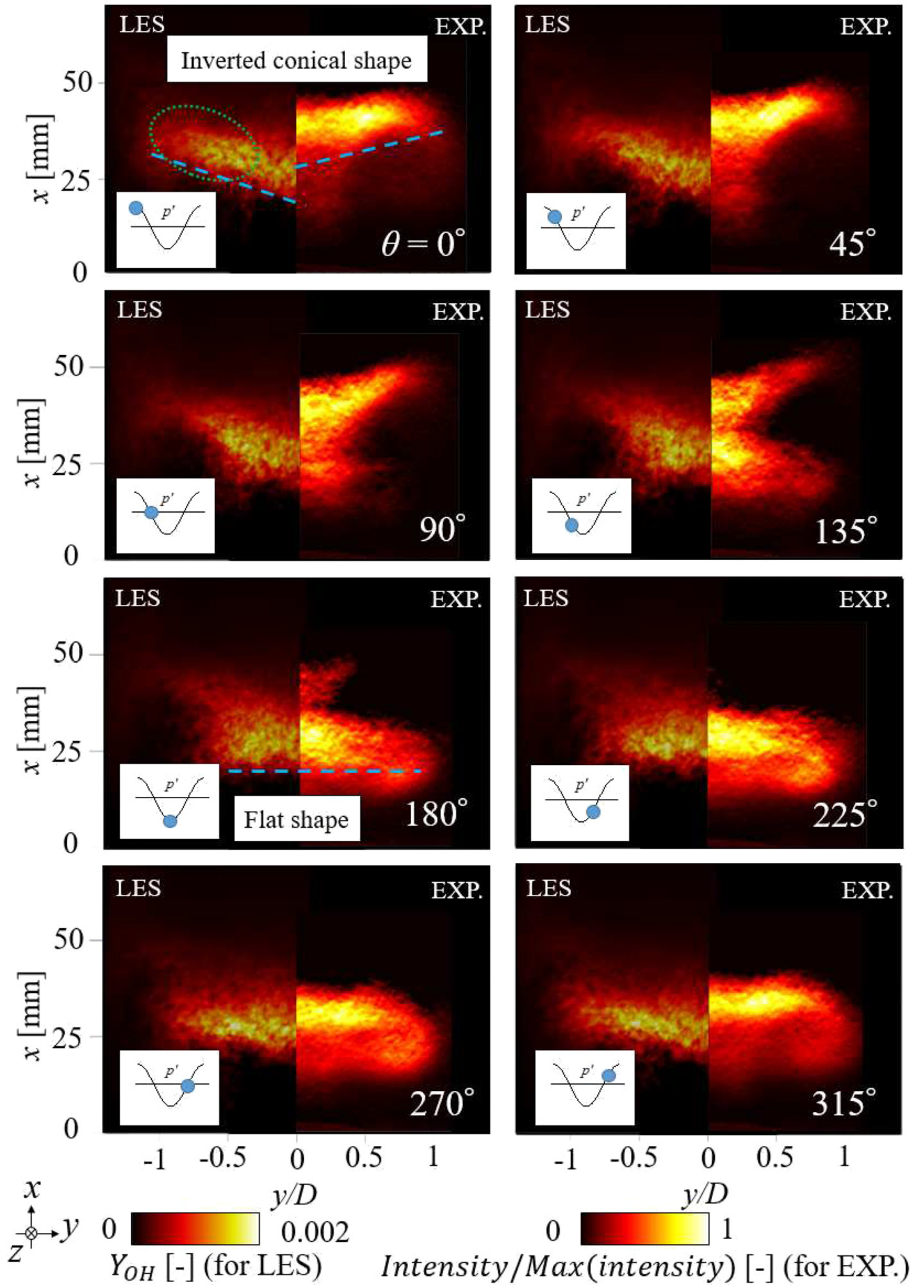

FIG. 13. Sequential images of the phase-averaged distribution of the mass fraction of OH, Y_{OH} on the x–y plane ($z = 0$ mm) at various phases with phase-averaged Abel-deconvoluted OH* chemiluminescence images from experimental results[30,31] (switching between the inverted conical and flat flame).

the experiment,[30,31] but was also not observed in the other paper, which also targeted the combustion instability in the low-swirl combustor.[69]

Furthermore, to examine the flame and inflow fluctuations in the CI in more detail, the fluctuations of the premixed gas supply from the injector are an essential factor, but it is superfluous to the main contents; therefore, the characteristics of inflow from the swirler to the flame surface are investigated in the Appendix.

A brief summary of this section is that the flame periodically transitions between the inverted conical flame and the flat flame, and it is attributed to the switching phenomenon under the CI, namely the outward and inward deflections of the inflow. These flame transitions and inflow switching phenomena are unique to this combustor configuration.

C. Flow switching phenomenon

As mentioned in Sec. III A, the pressure oscillates strongly under CI, and this affects the time variation of the velocity, namely, the outward and inward deflections of the inflow to the combustor, so-called flow switching phenomenon. To investigate the flow transitions inside

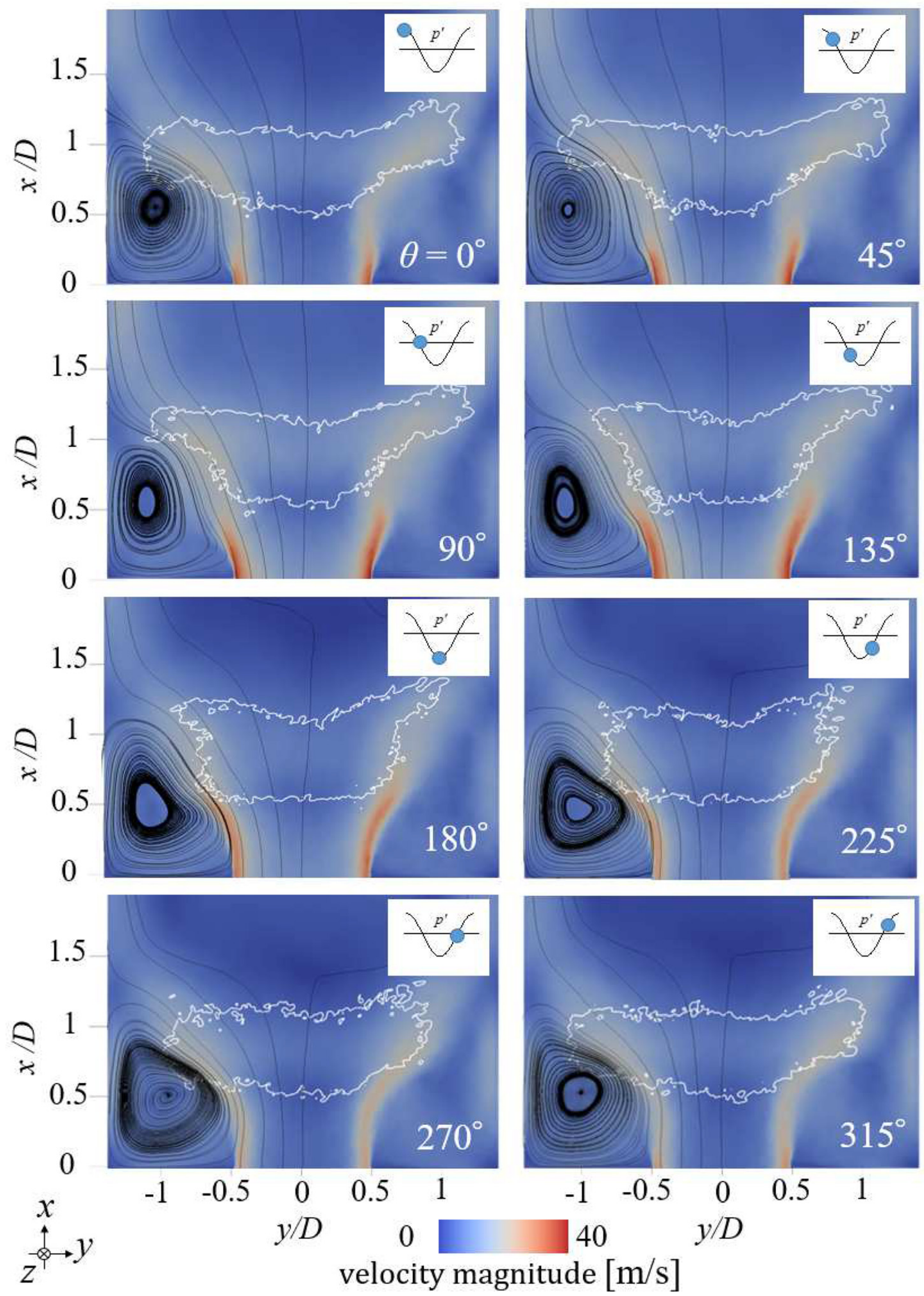

FIG. 14. Sequential images of the phase-averaged distribution of the velocity magnitude on the x–y plane ($z = 0$ mm) at various phases obtained from the LES. The white contours denote 20% of the maximum value of Y_{OH}, and the flow directions are represented by black lines (switching between the outward and inward deflections of inflow).

the combustor, it is necessary to know the inflow transition inside the inlet channel, and the transitions such as the acceleration and deceleration of inflow depend on the pressure gradient in the inlet channel. Therefore, to understand the time variation of the axial pressure distribution, Fig. 15 shows the phase-averaged pressure distribution in the streamwise direction at different phases obtained from the LES. In this figure, the positions α, β, and γ correspond to the positions indicated in Fig. 2. The amplitude of the pressure oscillations is found to be the largest around the swirler inlet (position α), which is the antinode of the oscillations, and its wavelength is about 3/4 of the length of the entire system comprising the injector and combustor, which is consistent with the estimation in the experiment.[30,31] Moreover, these positions of node and antinode are similar to that in the different study of the combustion instability in the low-swirl combustor[69] in which the antinode sits upstream of the inlet exit and node is positioned at the end of the combustor.

The pressure gradient in the inlet channel fluctuates and has positive and negative values, which accelerates and decelerates the inflow.

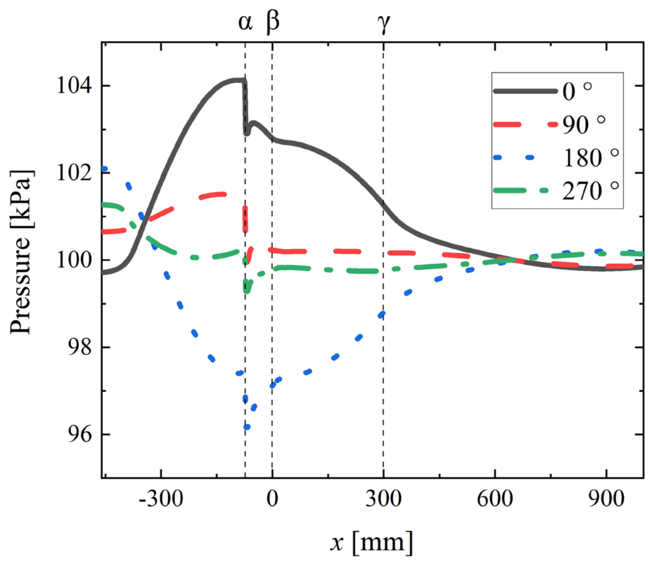

FIG. 15. Phase-averaged streamwise distributions of pressure at (y, z)=(0 mm, 0 mm) at $\theta = 0°, 90°, 180°, 270°$ obtained from the LES. Positions (α, β, γ) correspond to those indicated in Fig. 2.

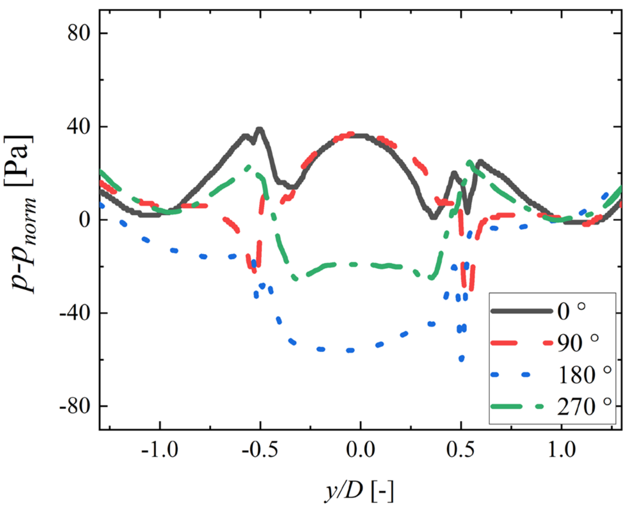

FIG. 17. Phase-averaged radial distributions of pressure, p, deducted by the pressure at $y/D = 1$, p_{norm}, at $\theta = 0°, 90°, 180°, 270°$ $(x, z) = (5\,\text{mm}, 0\,\text{mm})$ obtained from the LES (fluctuation of radial pressure gradient).

This fluctuating inflow affects the recirculating flow at the ORZ, and this subsequently affects the deflections of the inflow to the combustor. To examine the fluctuations of recirculating flow, Fig. 16 shows the sequential images of the phase-averaged distribution of the streamline in ORZ colored by the radial velocity, v, on the x–y plane ($z = 0$ mm) at various phases obtained from the LES. The scale and shape of the recirculating flow vary in tune with the pressure oscillation. When focusing on the distribution at around $\theta = 90°$, the major recirculating flow exists in the ORZ, and the shape of the recirculating flow is axially larger compared with the distributions at the other phases. Consequently, the radial velocity around the injector exit is relatively slow and has a small effect on the deflection of the inflow around this phase. Therefore, it forms the outwardly deflected inflow which is observed in the LSC with a stable operation. On the other hand, when focusing on the distribution at around $\theta = 270°$, the major recirculating flow shifts upstream and forms a radially larger recirculating flow compared with the distributions at the other phases. This distribution of recirculating flow makes the radial velocity faster in a broad region

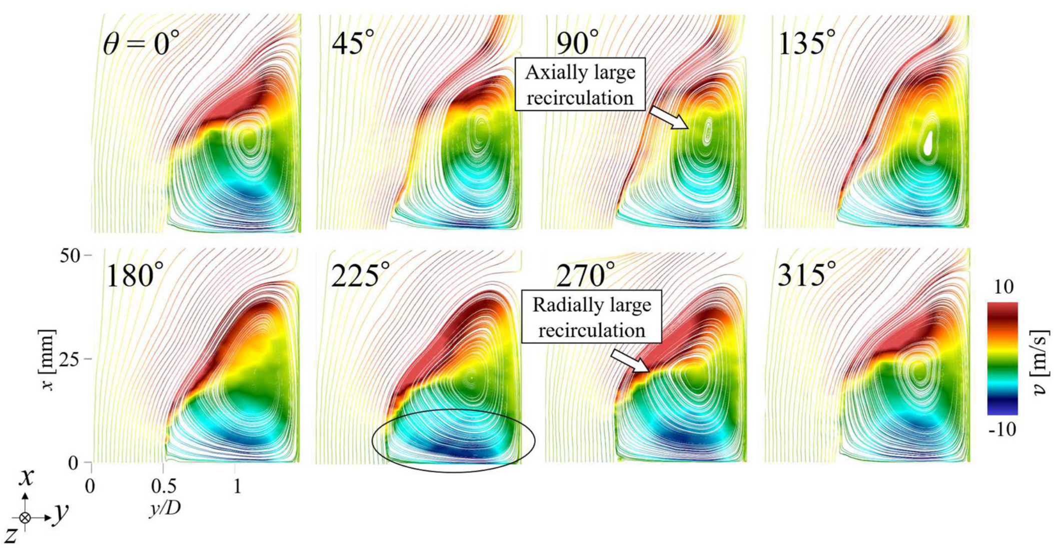

FIG. 16. Sequential images of the phase-averaged distribution of streamline in the ORZ colored by radial velocity, v, on the x–y plane ($z = 0$ mm) at various phases obtained from the LES (fluctuation of recirculating flow).

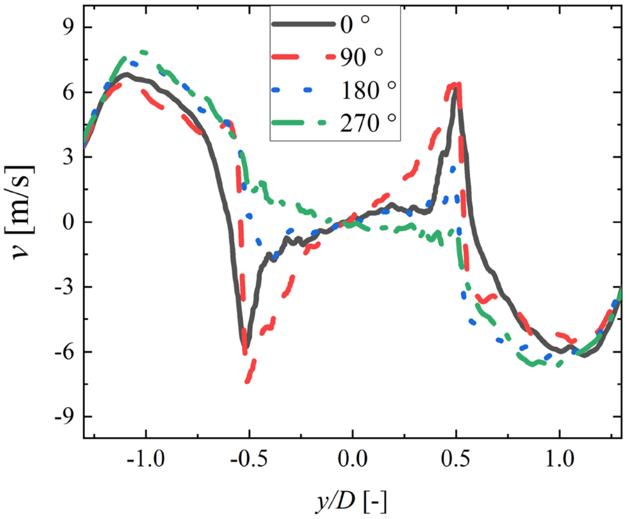

FIG. 18. Phase-averaged radial distributions of the radial velocity, v, at $\theta = 0°$, $90°$, $180°$, $270°$ $(x, z) = (5\,\text{mm}, 0\,\text{mm})$ obtained from the LES.

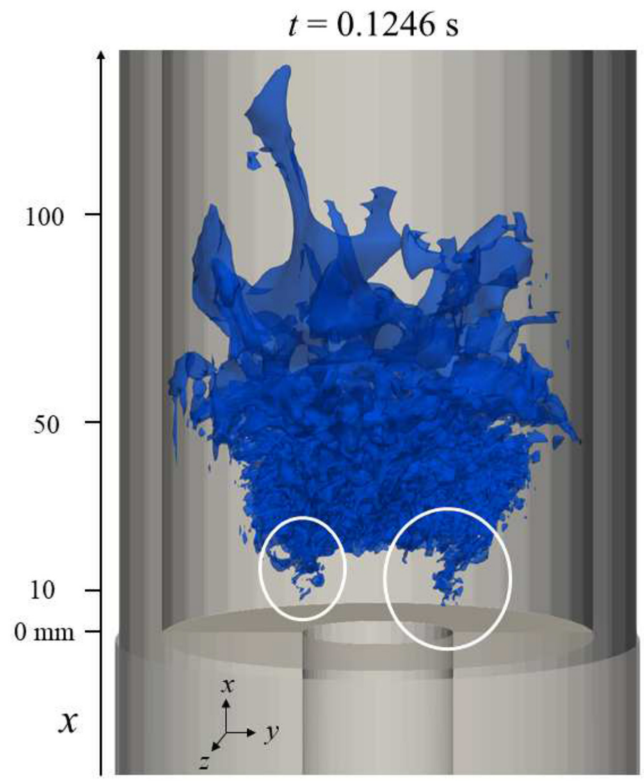

FIG. 19. Instantaneous 3D distribution of the isosurface of temperature at 1400 K (colored in blue) at the phase when the flame propagates upstream obtained from the LES (instantaneous flame's upstream extension).

around the injector exit [$0\,\text{mm} < x < 10\,\text{mm}$ and $0.5 < |y/D| < 1.4$ (circled in black in Fig. 16)] and the inflow deflect inwardly with respect to the streamwise direction.

In addition to the effect of the recirculating flow, the pressure distribution in the radial direction appears to be involved. Figure 17 shows the phase-averaged radial distributions of pressure at $x = 5$ mm deducted by the pressure at $y/D = 1$ different phases obtained from the LES. Once a resonant pressure oscillation occurs inside the combustor, the radial pressure distribution is not homogeneous, especially

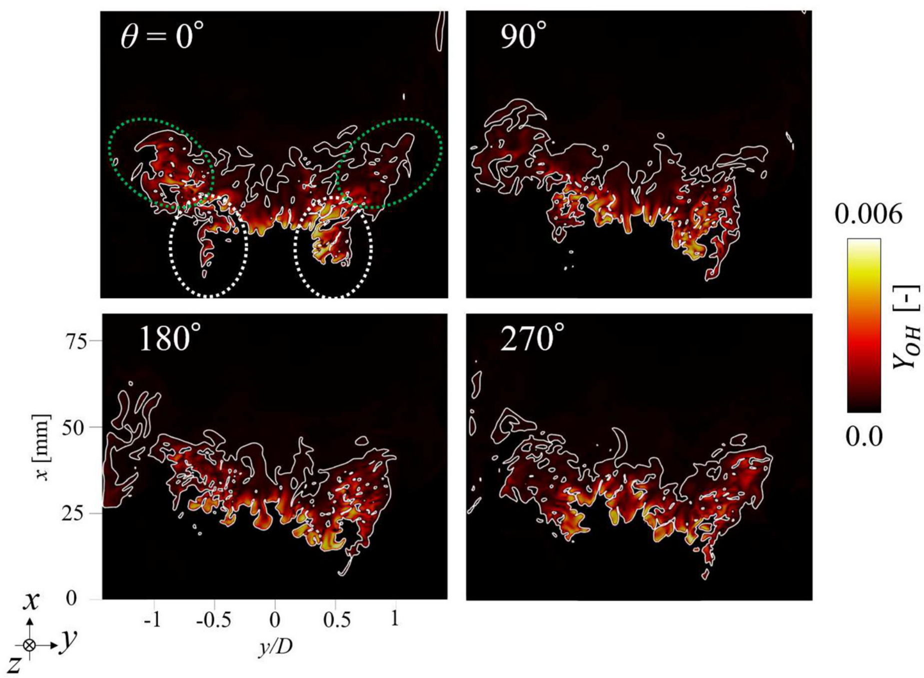

FIG. 20. Instantaneous distributions of the mass fraction of OH, Y_{OH} on the x–y plane ($z = 0$ mm) at $\theta = 0°, 90°, 180°, 270°$ obtained from the LES when the flame propagates to upstream. The white contours of 5% of the maximum value of Y_{OH} are also shown in this figure.

at the streamwise positions, such as at $x = 5$ mm, which are close to the injector exit. At phase $\theta = 0°$, the pressure around the combustor axis is higher than that around $y/D = 1$, and at $\theta = 180°$, the pressure around the combustor axis is lower than that around $y/D = 1$. Hence, at $\theta = 0°$, the positive radial pressure gradient induces the outward deflection of the inflow, and at $\theta = 180°$, the negative radial pressure gradient induces the inward deflection of the inflow.

Considering these effects mentioned above, the radial velocity must fluctuate, so the phase-averaged radial distributions of radial velocity at $x = 5$ mm at each phase obtained from the LES are shown in Fig. 18. Here, note that the phase difference between the oscillations of pressure and velocity is 90°. Thus, the velocity characteristics at phase $\theta = 90°$ can be analyzed using the pressure distribution at phase $\theta = 0°$. At phase $\theta = 90°$, the radial gradient of radial velocity, dv/dr, in the region $-0.5 < y/D < 0.5$ has a positive value, and it means that the flow is radially deflected outward, which is influenced by the fluctuation of recirculating flow and radial pressure distribution at phase $\theta = 0°$. In contrast, at phase $\theta = 270°$, dv/dr in the region $-0.5 < y/D < 0.5$ has a negative value, and this means that the flow is radially deflected inward.

In short summary, this section explores the unique switching phenomenon of the inflow, and it is found that the fluctuations of recirculating flow in the ORZ and of the radial pressure gradient have effects on the outward and inward deflections of the inflow. When the recirculating flow is strong and the radial pressure gradient is positive, the inflow points inward, and when the recirculating flow is weak and the radial pressure gradient is negative, the inflow points outward.

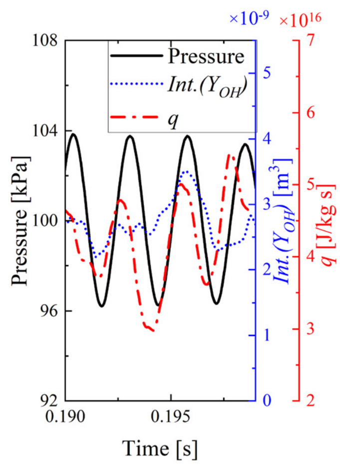

(a) With strong pressure oscillations

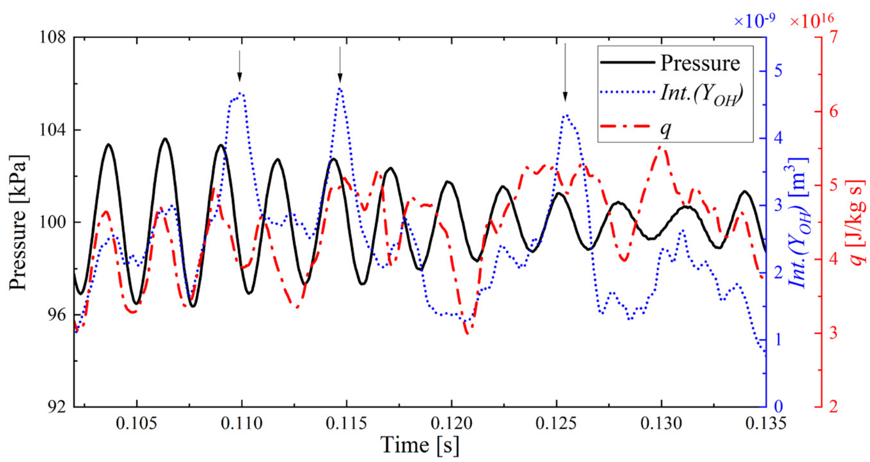

(b) With sporadic decay of pressure oscillations

FIG. 21. Short time series of pressure at point P (green square symbol in Fig. 2), integral of the mass fraction of OH upstream of combustor, $Int.(Y_{OH})$, and total heat release rate, q obtained from the LES (a) with strong pressure oscillations and (b) with sporadic decay of pressure oscillations (timing of the flame's upstream extension).

D. Instantaneous decay of pressure oscillations

The instantaneous decays of pressure oscillations as observed in Fig. 7 (indicated by the two black arrows) are discussed in detail. A comparison of the flame structures between the time duration when the amplitude of pressure oscillations is strong, and the time instance when the pressure oscillation amplitude declines sporadically is performed. Figure 19 shows the flame represented by an isosurface of temperature at 1400 K in the LSC obtained from the LES, which is colored in blue, at the time instance of $t = 0.1246$ s when the pressure oscillation amplitude is sporadically weakened. The flame structure when the pressure oscillates violently has already been presented in Fig. 4. When pressure oscillations sporadically decay, although the flame is lifted, it locally extends upstream in the areas circled in white.

To investigate the effect of such localized upstream flame propagation on the oscillatory phenomena, Fig. 20 shows the instantaneous Y_{OH} distributions on the x–y plane at different phases obtained from the LES during the time period when the pressure oscillation amplitude is sporadically weakened. In this figure, it is once again confirmed that the flame locally extends upstream in the areas circled by white dotted lines. In addition, judging from the flame fluctuation phenomenon, when strong pressure oscillations occur in the combustor, the flame structure periodically transitions between the inverted conical shape and the flat shape, as shown in Fig. 13, whereas when the amplitude of the pressure oscillations is weak, the flame structure transition is not observed at any phase. This is because the localized upstream extension of the flame stabilizes the flame structure and prevents its violent fluctuations, thereby causing the flame to always be present in the areas outlined by the green dotted lines in Fig. 20. This results in a weakening of the correlation between pressure oscillations and heat release rate fluctuations in these regions where the local *RI* would otherwise be high under strong CI conditions (i.e., drastic flame fluctuations).

To investigate the timing of the occurrence of this sporadic flame extension during the strong pressure oscillation, Fig. 21 shows the LES result of the time series of pressure and the mass fraction of OH integrated spatially, $Int.(Y_{OH})$, over the combustor volume ranging from $x = 0$ to $x = 17$ mm, which is the upstream region of the flame, when pressure oscillates strongly and when the pressure oscillations instantaneously decay. In the time interval with the strong pressure oscillation, $Int.(Y_{OH})$ oscillates in phase with the pressure oscillation, and at the phase when the pressure becomes maximum, $Int.(Y_{OH})$ also has a maximum value. On the other hand, in the time interval with weak pressure oscillation, at some time instances, $Int.(Y_{OH})$ spikes up and becomes much higher than other time instances, as pointed by the black arrows, which indicate the existence of the eminent flame extension to the upstream. Moreover, the spikes of $Int.(Y_{OH})$ oscillation lag the pressure oscillation peaks compared with the other peaks of $Int.(Y_{OH})$. To understand the impact of the flame extension on the coupling between the pressure oscillations and the heat release rate fluctuations, the total heat release rates are also shown in Fig. 21. After the first spike of $Int.(Y_{OH})$, the phase difference between the pressure oscillations and the fluctuations of heat release rate increases, suggesting a decoupling of these two fluctuations. Moreover, after the second spike of $Int.(Y_{OH})$, the heat release rate does not fluctuate in synchrony with the pressure oscillations, which induces the pressure oscillation to decay more.

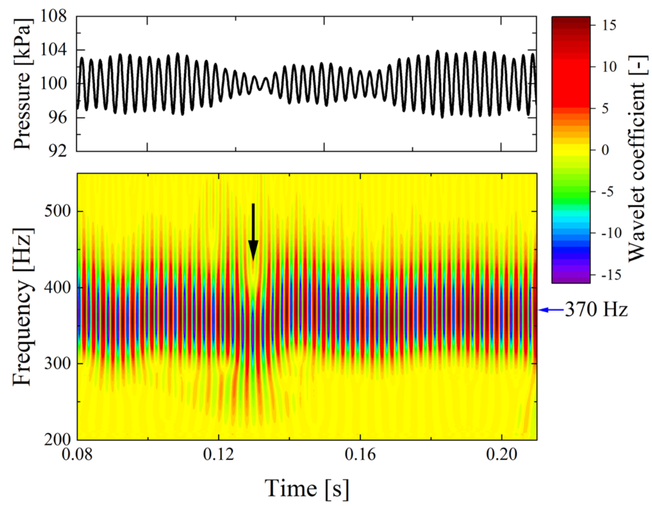

FIG. 22. Time series of the pressure oscillation and its frequency obtained by the wavelet analysis using the data obtained from the LES (frequency shift during the pressure oscillation decay).

Furthermore, in the process of instantaneous decay of pressure oscillation, the pressure oscillation is considered to deviate from the resonant mode of the combustor. Therefore, to investigate the mode shift, the wavelet analysis is employed. Here, as the wavelet type, Morlet is used, and the wave number is set to 10. Figure 22 shows the time series of the pressure oscillation and its frequency. As predicted, when the pressure instantaneously decays, as pointed out by a black arrow, the pressure oscillation frequency becomes lower compared with the resonant frequency, 370 Hz. As a result, the pressure oscillation decays, but once the pressure oscillation frequency gets back to the resonant frequency, the amplitude of the pressure oscillation becomes stronger again.

All in all, without the flame extension, the incoming unburned premixed gas is entrained in the oscillating lifted flame, and the phase difference between pressure and heat release rate became such that the RI increased, thus maintaining combustion oscillation. However, with the flame extension, combustion occurs further upstream, and the phase difference between pressure and heat release rate changes, resulting in a smaller RI and the inability to generate enough energy to maintain the thermoacoustic. This is because the localized upstream extension of the flame stabilizes the flame structure and prevents its violent fluctuations. This localized flame extension in the upstream direction can occur at any time, but whether or not the reactions occur actively enough in the upstream regions to enable the localized upstream flame propagation and stabilization of the fluctuations of the flame structure is primarily determined by various factors, including the amount of hot gas entrained locally toward the combustor axis, amount of unburned premixed gas coming into contact with the hot gas, and local flow-field conditions.

IV. CONCLUSIONS

In this study, the mechanism of flame-flow dynamics of a lean-premixed hydrogen flame in a low-swirl combustor (LSC) under combustion instability was investigated in detail using LES, which considered the swirler assembly in the upstream region (i.e., injector). As a combustion model, a dynamically thickened flame model[42–46] with a detailed chemical reaction model consisting of 9 chemical species and 20 reactions[48] was employed. The configurations of the combustor and injector were the same as those in the experiment.[30,31] The swirl number of the swirler in the injector was set to be about 0.39, the bulk velocity in the injector channel was 15 m/s, the pressure was 0.1 MPa, the length of the combustor was 300 mm, and the equivalence ratio was 0.39. The main results of this study are summarized as follows.

1. The present LES predicts the combustion instability phenomena observed in the experiment.[30,31] Namely, the pressure inside the LSC strongly oscillates, and the pressure oscillations' frequency and intensity are in quantitatively good agreement with that in the experiment.[30,31] Moreover, although the pressure oscillations sporadically exhibit temporal declines in amplitude, they are not fully damped but recover again. Furthermore, a unique behavior, which was first confirmed in the experiment,[30,31] such as the periodic transitions between the inverted conical flame structure and the flat flame structure, is similarly observed.
2. The periodic transitions between the inverted conical flame structure and flat flame structure are caused by the outward and inward deflections of the inflow, which is comprehensively associated with the fluctuation of the recirculating flow behavior in the region near the combustor wall, the pressure gradient in the radial direction inside the combustor, and the flow behavior in the upstream injector channel. Specifically, the inverted conical flame is formed by the outward deflection of the inflow with a faster velocity, which pushes the flame in the radially outer region downstream. On the other hand, the flat flame is formed by the inward deflection of the inflow with slower velocity, which allows the flame in the radially outer region to propagate upstream.
3. The sporadic decay of pressure oscillations mentioned in conclusion 1 appears when the pressure oscillations and heat release rate fluctuations temporally decouple. This temporal decoupling is caused by the aperiodic flame transformation, namely, the flame temporally and locally propagates toward the upstream region close to the rim of the injector, which makes the flame stable.

ACKNOWLEDGMENTS

This work was partially supported by JSPS KAKENHI (Grant No. 22H00192) and by MEXT as "Program for Promoting Researches on the Supercomputer Fugaku" (Development of the Smart design system on the supercomputer "Fugaku" in the era of Society 5.0) (No. JPMXP1020210316). This research used the computational resources of supercomputer Fugaku provided by the RIKEN Center for Computational Science (Project ID: hp200160, hp210020, and hp220004).

AUTHOR DECLARATIONS

Conflict of Interest

The authors have no conflicts to disclose.

Author Contributions

Jun Nagao: Formal analysis (equal); Investigation (equal); Methodology (equal); Software (equal); Validation (equal); Visualization (equal); Writing – original draft (equal); Writing – review & editing (equal). **Abhishek Lakshman Pillai:** Software (equal); Writing – original draft (equal); Writing – review & editing (equal). **Takeshi Shoji:** Conceptualization (equal); Formal analysis (equal); Investigation (equal). **Shigeru Tachibana:** Conceptualization (equal); Formal analysis (equal); Investigation (equal). **Takeshi Yokomori:** Conceptualization (equal); Formal analysis (equal); Investigation (equal). **Ryoichi Kurose:** Conceptualization (equal); Formal analysis (equal); Funding acquisition (equal); Investigation (equal); Project administration (equal); Supervision (equal).

DATA AVAILABILITY

The data that support the findings of this study are available within the article.

APPENDIX: DELAY TIME OF INFLOW

As mentioned above, the fluctuations of the premixed gas supply from the injector are an essential factor. In this study, the particle tracking method is employed to capture the inflow characteristics, and the trajectory and the delay time, which denote the travel time of a particle, are investigated.

The following procedure is applied as the particle tracking method. Approximately 5000 particles are placed spatially homogeneously on the y–z plane ($x = -80$ mm) upstream of the swirler in the injector tube at phase $\theta = 0°$. Each particle convects with the velocity of the premixed gas downstream. This procedure is applied as the post-process of the LES, and these particles do not affect the turbulent combustion field. The delay time, τ_{-80}, is estimated as the required time to come to certain positions from $x = -80$ mm. In this analysis, the delay time of particles at $x = -40$ mm, $x = 0$ mm, and on the flame surface is investigated. The flame surface is defined as the position of 5% of the maximum OH mass fraction ($Y_{OH,5\%} = 3 \times 10^{-4}$). The required time for a particle to come to a certain position is measured only when the particle reaches the position, and thus, it can be presumed that all particles which are used to calculate the delay time are in the unburnt gas. In the experiment, a similar analysis was conducted, but the delay time was estimated as the travel time from $x = 0$ mm to the flame surface, because no data were available in the injector channel. Therefore, to compare the LES results with the experimental results, τ_0 is also calculated using this LES data.

Figure 23 shows the initial distribution and sequential images of particles with the flame surface represented by the blue isosurfaces, which denote the 5% of the maximum OH mass fraction ($Y_{OH,5\%} = 3 \times 10^{-4}$). The colors of particles represent the initial radial distance from the combustor axis at $x = -80$ mm, r_{-80}. As this figure shows, the particles convect downstream and flow into the combustor. Some particles are trapped and do not move on the wall surface due to the presumption of the non-slip wall, but the number of trapped particles is not so significant that it can derail the discussion. Most particles which flow into the combustor spread

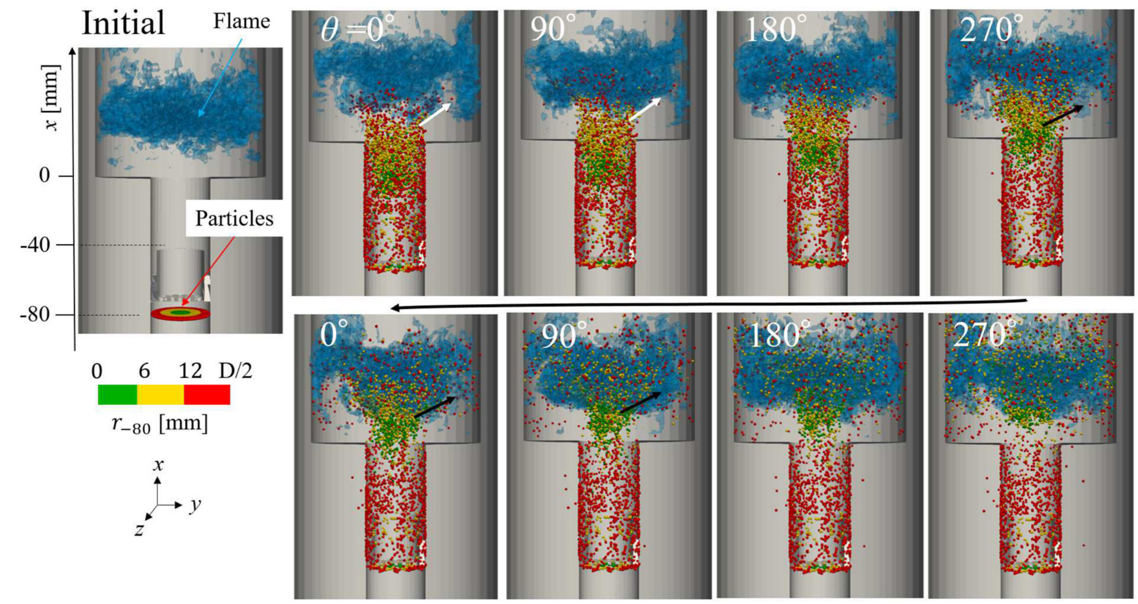

FIG. 23. Initial distribution and sequential images of particles for calculating the delay time, τ. The blue isosurfaces denote the 5% of the maximum OH mass fraction ($Y_{OH,5\%} = 3 \times 10^{-4}$), and all particles are colored by the initial radial distance from the combustor axis at $x = -80$ mm, r_{-80}.

in a radially outward direction and pass through the flame surface, but different particle motions are observable among the particles from different initial positions.

To investigate the various particle motions, Fig. 24 shows the scatterplot of delay time, τ_{-80}, at $x = -40$ mm, $x = 0$ mm, and on the flame surface, and τ_0. In this figure, the wall position, W.P., is depicted with a black line. As this figure shows, the delay time from $x = -80$ to $x = -40$ mm is almost the same among the radial locations, but the delay time from $x = -80$ to $x = 0$ mm is longer around the center axis of the combustor than that at the peripheral of the injector ($|r/D| \approx 0.5$). This is attributed to the velocity distribution in the injector channel, in which the velocity at the center axis is slower than the peripheral of the injector.

On the other hand, the distribution of delay time on the flame surface from $x = -80$ mm is considerably different from the other axial positions. The delay time is longer around the center axis of the combustor, and it becomes the shortest around $r/D = 0.5$ and increases at the region $r/D > 0.5$. At the region $r/D > 0.5$, as pointed out by two red arrows, the distribution is split into two parts, which means that the particles go through the flame surface not constantly but periodically, even though the particles enter the flame surface constantly in the other regions. This periodic entry of particles, which consequently represents the supply of the unburnt premixed gas to the flame surface in the ORZ, $r/D > 0.5$, makes the local RI larger at this region, as shown in Fig. 12, and the constant entry around the center axis makes the local RI smaller. For the two split distributions at $r/D > 0.5$ pointed out by the two red arrows in Fig. 24(c), this time difference is almost the same as the time for a single cycle of pressure oscillation (≈ 2.7 ms), and the underlying phenomena are tightly connected with the thermal–acoustic coupling. Furthermore, the first distribution of the two split distributions at $r/D > 0.5$ ($\tau_{-80} \approx 6$ ms) mainly consists of red particles, which means that particles originally in the peripheral region of the injector go through the flame surface first, and the second distribution of the two split distributions at $r/D > 0.5$ ($\tau_{-80} \approx 8$ ms) also consists of yellow and green particles, which means that particles originally in the center region of the injector go through the flame surface at the next cycle after the cycle when the particles originally at the peripheral region of the injector go through the flame surface. These characteristics are also confirmed in Fig. 23. In the first cycle, the yellow and green particles are yet to pass through the flame surface at $r/D > 0.5$, but the red particles move toward the flame surface as indicated by white arrows with the vortex as shown in Fig. 14. In the second cycle, the yellow and green particles which have flown into the central region in the combustor are transferred radially outward in the combustor, as indicated by black arrows, and they pass through the flame surface at $r/D > 0.5$. However, a relatively small amount of green particles are distributed $r/D > 0.5$ in the second cycle, and the green particles at $r/D < 0.5$ have a wider range of delay time, which represents the small effect of the premixed gas originally in the center region of the injector on the CI.

In addition to the above discussion, a comparison with the experiment is performed. When the delay time on the flame surface is calculated with particles originating from $x = 0$ mm, the delay time, τ_0, becomes minimum around $r/D = 0.5$. This is similar to the experimental results.[31] However, contrary to the trend of the time delay from $x = -80$ mm, τ_{-80}, most particles go through the flame surface at the same delay time. This is because when the delay time is measured from the time at the $x = 0$ mm, the residence time of particles inside the injector channel cannot be captured. Therefore, to investigate the different inflow characteristics under the CI in this configuration, it is indispensable to consider the fluctuations of flow inside the injector.

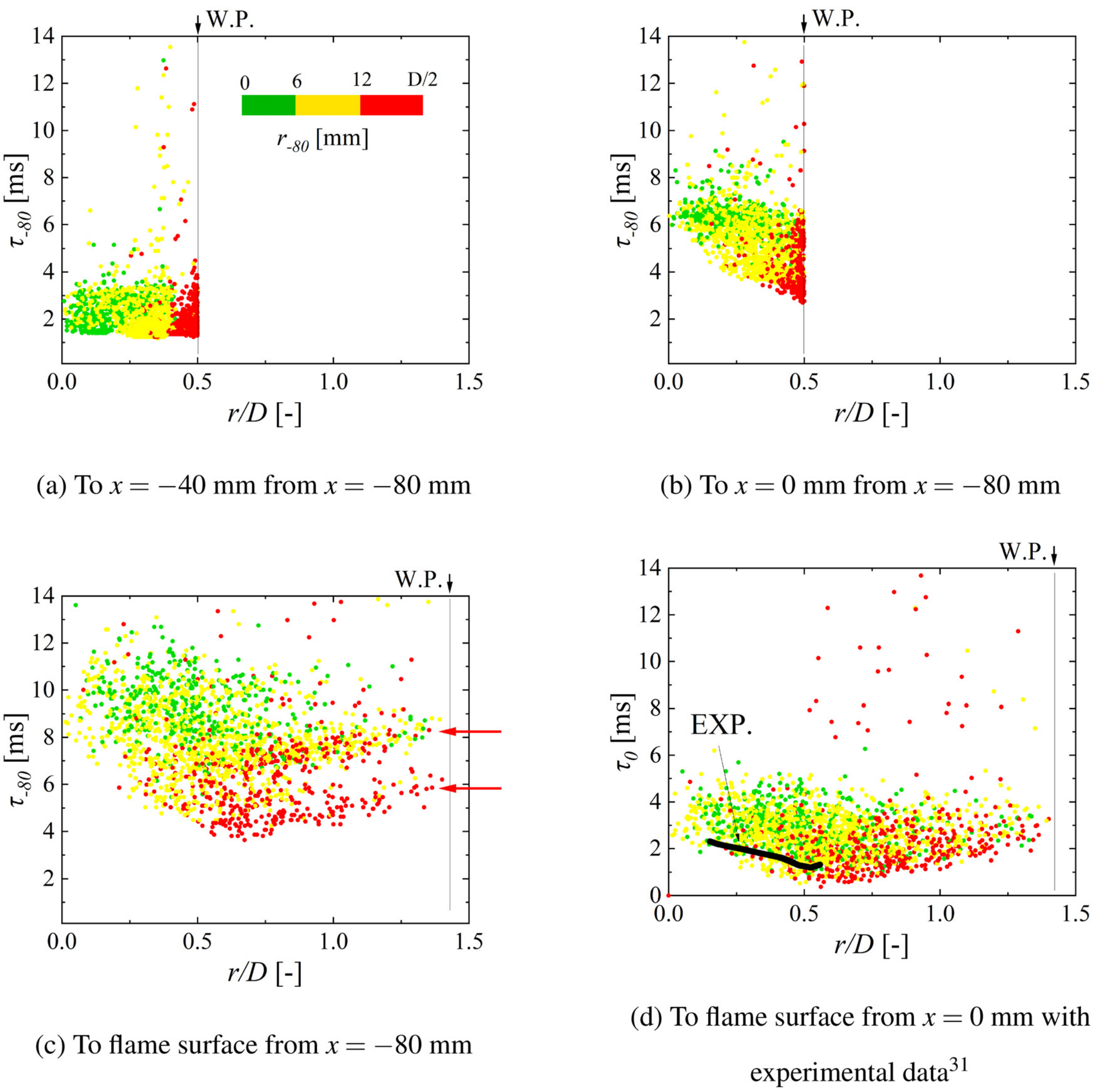

(a) To $x = -40$ mm from $x = -80$ mm

(b) To $x = 0$ mm from $x = -80$ mm

(c) To flame surface from $x = -80$ mm

(d) To flame surface from $x = 0$ mm with experimental data[31]

FIG. 24. Comparison of the scatter plots of delay time, τ, (a) to $x = -40$ mm from $x = -80$ mm, (b) to $x = 0$ mm from $x = -80$ mm, (c) to flame surface from $x = -80$ mm, and (d) to flame surface from $x = 0$ mm with experimental data.[31] The subscript of τ denotes the axial reference position of the delay time, and the radial wall position, W.P., is also depicted with plots. All particles are colored by the initial radial distance from the combustor axis at $x = -80$ mm, r_{-80}.

REFERENCES

[1]R. E. Jones, "Gas turbine engine emissions–problems, progress and future," Prog. Energy Combust. Sci. **4**, 73–113 (1978).

[2]N. A. Cumpsty, "Preparing for the future: Reducing gas turbine environmental impact—IGTI scholar lecture," J. Turbomach. **132**, 041017 (2010).

[3]A. Gupta, "Thermal characteristics of gaseous fuel flames using high temperature air," J. Eng. Gas Turbines Power **126**, 9–19 (2004).

[4]R. Pavri and G. D. Moore, "Gas turbine emissions and control," in Proceedings of the GE Energy Services (2001).

[5]A. Gupta, "Gas turbine combustion: Prospects and challenges," Energy Convers. Manage. **38**, 1311–1318 (1997).

[6]ICAO, see http://www.icao.int/Pages/default.aspx for "Icao" (2010) (last accessed May 15, 2023).

[7]F. Ommi and M. Azimi, "Most effective combustion technologies for reducing NO_x emissions in aero gas turbines," Int. J. Multiphys. **6**, 417 (2012).

[8]T. Lieuwen and K. McManus, "Introduction: Combustion dynamics in lean-premixed prevaporized (LPP) gas turbines," J. Propul. Power **19**, 721 (2003).

[9]C. Eichler, G. Baumgartner, and T. Sattelmayer, "Experimental investigation of turbulent boundary layer flashback limits for premixed hydrogen-air flames confined in ducts," J. Eng. Gas Turbines Power **134**, 011502 (2012).

[10]A. Gruber, J. Chen, D. Valiev, and C. Law, "Direct numerical simulation of premixed flame boundary layer flashback in turbulent channel flow," J. Fluid Mech. **709**, 516–542 (2012).

[11]T. Kitano, T. Tsuji, R. Kurose, and S. Komori, "Effect of pressure oscillations on flashback characteristics in a turbulent channel flow," Energy Fuel **29**, 6815–6822 (2015).

[12]D. Ebi, R. Bombach, and P. Jansohn, "Swirl flame boundary layer flashback at elevated pressure: Modes of propagation and effect of hydrogen addition," Proc. Combust. Inst. **38**, 6345–6353 (2021).
[13]L. Esclapez, P. Ma, E. Mayhew, R. Xu, S. Stouffer, T. Lee, H. Wang, and M. Ihme, "Fuel effects on lean blow-out in a realistic gas turbine combustor," Combust. Flame **181**, 82–99 (2017).
[14]L. Zheng, J. Cronly, E. Ubogu, I. Ahmed, Y. Zhang, and B. Khandelwal, "Experimental investigation on alternative fuel combustion performance using a gas turbine combustor," Appl. Energy **238**, 1530–1542 (2019).
[15]A. Aniello, T. Poinsot, L. Selle, and T. Schuller, "Hydrogen substitution of natural-gas in premixed burners and implications for blow-off and flashback limits," Int. J. Hydrogen Energy **47**, 33067–33081 (2022).
[16]T. Lieuwen and V. Yang, *Combustion Instabilities in Gas Turbine Engines: Operational Experience, Fundamental Mechanisms and Modeling* (Progress in Astronautics and Aeronautics, 2005).
[17]L. Rayleigh, "The explanation of certain acoustical phenomena," Nature **18**, 319–321 (1878).
[18]T. Poinsot, D. Haworth, and G. Bruneaux, "Direct simulation and modeling of flame-wall interaction for premixed turbulent combustion," Combust. Flame **95**, 118–132 (1993).
[19]A. Dreizler and B. Böhm, "Advanced laser diagnostics for an improved understanding of premixed flame-wall interactions," Proc. Combust. Inst. **35**, 37–64 (2015).
[20]R. Kai, A. L. Pillai, U. Ahmed, N. Chakraborty, and R. Kurose, "Analysis of the evolution of the surface density function during premixed v-shaped flame-wall interaction in a turbulent channel flow at $Re_\tau = 395$," Combust. Sci. Technol. 1–27 (2022).
[21]J. Park and M. Lee, "Combustion instability characteristics of H_2/CO/CH_4 syngases and synthetic natural gases in a partially-premixed gas turbine combustor: Part I—Frequency and mode analysis," Int. J. Hydrogen Energy **41**, 7484–7493 (2016).
[22]J. Nam and J. Yoh, "A numerical investigation of the effects of hydrogen addition on combustion instability inside a partially-premixed swirl combustor," Appl. Therm. Eng. **176**, 115478 (2020).
[23]U. Jin and K. Kim, "Influence of radial fuel staging on combustion instabilities and exhaust emissions from lean-premixed multi-element hydrogen/methane/air flames," Combust. Flame **242**, 112184 (2022).
[24]R. Smith, G. Xia, W. A. Anderson, and C. L. Merkle, "Computational simulations of the effect of backstep height on nonpremixed combustion instability," AIAA J. **48**, 1857–1868 (2010).
[25]J. Sisco, Y. Yu, V. Sankaran, and W. Anderson, "Examination of mode shapes in an unstable model combustor," J. Sound Vib. **330**, 61–74 (2011).
[26]F. Culick, M. Heitor, and J. Whitelaw, *Unsteady Combustion* (Springer Science & Business Media, 1996).
[27]M. Zhu, A. Dowling, and K. Bray, "Self-excited oscillations in combustors with spray atomizers," J. Eng. Gas Turbines Power **123**, 779–786 (2001).
[28]J.-Y. Lee, E. Lubarsky, and B. Zinn, "'Slow' active control of combustion instabilities by modification of liquid fuel spray properties," Proc. Combust. Inst. **30**, 1757–1764 (2005).
[29]M. de la Cruz García, E. Mastorakos, and A. Dowling, "Investigations on the self-excited oscillations in a kerosene spray flame," Combust. Flame **156**, 374–384 (2009).
[30]T. Shoji, S. Tachibana, T. Suzuki, Y. Nakazumi, and T. Yokomori, "A new pattern of flame/flow dynamics for lean-premixed, low-swirl hydrogen turbulent jet flames under thermoacoustic instability," Proc. Combust. Inst. **38**, 2835–2843 (2021).
[31]T. Shoji, S. Tachibana, Y. Nakazumi, R. Fujii, J. Masugi, and T. Yokomori, "Detailed unsteady dynamics of flame-flow interactions during combustion instability and its transition scenario for lean-premixed low-swirl hydrogen turbulent flames," Proc. Combust. Inst. **39**, 4741–4750 (2023).
[32]K. Moon, Y. Choi, and K. Kim, "Experimental investigation of lean-premixed hydrogen combustion instabilities in a can-annular combustion system," Combust. Flame **235**, 111697 (2022).
[33]B. Franzelli, E. Ribera, L. Gicquel, and T. Poinsot, "Large eddy simulation of combustion instabilities in a lean partially premixed swirled flame," Combust. Flame **159**, 621–637 (2012).
[34]S. Tachibana, K. Saito, T. Yamamoto, M. Makida, T. Kitano, and R. Kurose, "Experimental and numerical investigation of thermo-acoustic instability in a liquid-fuel aero-engine combustor at elevated pressure: Validity of large-eddy simulation of spray combustion," Combust. Flame **162**, 2621–2637 (2015).
[35]T. Kitano, K. Kaneko, R. Kurose, and S. Komori, "Large-eddy simulations of gas- and liquid-fueled combustion instabilities in back-step flows," Combust. Flame **170**, 63–78 (2016).
[36]J. Li, Y. Xia, A. S. Morgans, and X. Hanc, "Numerical prediction of combustion instability limit cycle oscillations for a combustor with a long flame," Combust. Flame **185**, 28–43 (2017).
[37]C. Kraus, L. Selle, and T. Poinsot, "Coupling heat transfer and large eddy simulation for combustion instability prediction in a swirl burner," Combust. Flame **191**, 239–251 (2018).
[38]A. Pillai, J. Nagao, R. Awane, and R. Kurose, "Influences of liquid fuel atomization and flow rate fluctuations on spray combustion instabilities in a backward-facing step combustor," Combust. Flame **220**, 337–356 (2020).
[39]L. Yuanzhe, L. P. nad, W. Zhuopu, A. Wen, and G. Yu, "Large eddy simulation of combustion instability in a subcritical hydrogen peroxide/kerosene liquid rocket engine: Intermittency route to period-2 thermoacoustic instability," Phys. Fluids **35**, 065145 (2023).
[40]R. Cheng, D. Yegian, M. Miyasato, G. Samuelsen, C. Benson, R. Pellizzari, and P. Loftus, "Scaling and development of low-swirl burners for low-emission furnaces and boilers," Proc. Combust. Inst. **28**, 1305–1313 (2000).
[41]R. Cheng, D. Littlejohn, P. Strakey, and T. Sidwell, "Laboratory investigations of a low-swirl injector with H_2 and CH_4 at gas turbine conditions," Proc. Combust. Inst. **32**, 3001–3009 (2009).
[42]J.-P. Légier, T. Poinsot, and D. Veynante, "Dynamically thickened flame LES model for premixed and non-premixed turbulent combustion," in *Proceedings of the Summer Program* (Standord, 2000), pp. 157–168.
[43]F. Charlette, C. Meneveau, and D. Veynante, "A power-law flame wrinkling model for LES of premixed turbulent combustion Part I: Non-dynamic formulation and initial tests," Combust. Flame **131**, 159–180 (2002).
[44]P. Strakey and G. Eggenspieler, "Development and validation of a thickened flame modeling approach for large eddy simulation of premixed combustion," J. Eng. Gas Turbines Power **132**, 071501 (2010).
[45]F. Proch and A. Kempf, "Numerical analysis of the Cambridge stratified flame series using artificial thickened flame LES with tabulated premixed flame chemistry," Combust. Flame **161**, 2627–2646 (2014).
[46]A. Rittler, F. Proch, and A. Kempf, "LES of the Sydney piloted spray flame series with the PFGM/ATF approach and different sub-filter models," Combust. Flame **162**, 1575–1598 (2015).
[47]O. Colin, F. Ducros, D. Veynante, and T. Poinsot, "A thickened flame model for large eddy simulations of turbulent premixed combustion," Phys. Fluids **12**, 1843 (2000).
[48]J. A. Miller and C. T. Bowman, "Mechanism and modeling of nitrogen chemistry in combustion," Prog. Energy Combust. Sci. **15**, 287–338 (1989).
[49]V. Moureau, C. Berat, and H. Pitsch, "An efficient semi-implicit compressible solver for large-eddy simulations," J. Comput. Phys. **226**, 1256–1270 (2007).
[50]J. Nagao, A. Pillai, T. Shoji, S. Tachibana, T. Yokomori, and R. Kurose, "Numerical investigation of wall effects on combustion noise from a lean-premixed hydrogen/air low-swirl flame," Phys. Fluids **35**, 014109 (2022).
[51]R. Kai, T. Tokuoka, J. Nagao, A. Pillai, and R. Kurose, "LES flamelet modeling of hydrogen combustion considering preferential diffusion effect," Int. J. Hydrogen Energy **48**, 11086–11101 (2023).
[52]F. Williams, *Combustion Theory* (The Benjamin/Cummings Publishing Company, 1985).
[53]A. Ern and V. Giovangigli, *Multicomponent Transport Algorithms* (Springer, 1994).
[54]R. J. Kee, J. A. Miller, and T. H. Jefferson, "CHEMKIN: A general-purpose, problem-independent, transportable, FORTRAN chemical kinetics code package," Report No. SAND 80-8003, 1980.
[55]P. Moin, K. Squires, W. Cabot, and S. Lee, "A dynamic subgrid-scale model for compressible turbulence and scalar transport," Phys. Fluids **3**, 2746–2757 (1991).

[56] C. Pierce and P. Moin, "A dynamic model for subgrid-scale variance and dissipation rate of a conserved scalar," Phys. Fluids **10**, 3041–3044 (1998).
[57] A. Pillai, S. Inoue, T. Shoji, S. Tachibana, T. Yokomori, R. Awane, and R. Kurose, "Investigation of combustion noise generated by an open lean-premixed H_2/air low-swirl flame using the hybrid LES/APE-RF framework," Combust. Flame **245**, 112360 (2022).
[58] R. Kurose, see http://www.tse.me.kyoto-u.ac.jp/members/kurose/link_e.php (2022) for "In-house code FK^3" (last accessed May 15, 2023).
[59] T. Kawamura, H. Takami, and K. Kuwahara, "Computation of high Reynolds number flow around a circular cylinder with surface roughness," Fluid Dyn. Res. **1**, 145–162 (1986).
[60] G.-S. Jiang and C.-W. Shu, "Efficient implementation of weighted ENO schemes," J. Comput. Phys. **126**, 202–228 (1996).
[61] M. Day, S. Tachibana, J. Bell, M. Lijewski, V. Beckner, and R. Cheng, "A combined computational and experimental characterization of lean premixed turbulent low swirl laboratory flames II. Hydrogen flames," Combust. Flame **162**, 2148–2165 (2015).
[62] J. Bell, R. Cheng, M. Day, and I. Sheperd, "Numerical simulation of Lewis number effects on lean premixed turbulent flames," Proc. Combust. Inst. **31**, 1309–1317 (2007).
[63] J. Bell, M. Day, and M. Lijewski, "Simulation of nitrogen emissions in a premixed hydrogen flame stabilized on a low swirl burner," Proc. Combust. Inst. **34**, 1173–1182 (2013).
[64] S. Schlimpert, S. Koh, K. Pausch, M. Meinke, and W. Schröder, "Analysis of combustion noise of a turbulent premixed slot jet flame," Combust. Flame **175**, 292–306 (2017).
[65] R. Rajaram and T. Lieuwen, "Acoustic radiation from turbulent premixed flames," J. Fluid Mech **637**, 357–385 (2009).
[66] K. Pausch, S. Schlimpert, S. Koh, J. Grimmen, and W. Schröder, "The effect of flame thickening on the acoustic emission in turbulent combustion," AIAA Paper No. 2016-2745, 2016.
[67] Y. Hardalupas and M. Orain, "Local measurements of the time-dependent heat release rate and equivalence ratio using chemiluminescent emission from a flame," Combust. Flame **139**, 188–207 (2004).
[68] C. Panoutsos, Y. Hardalupas, and A. Taylor, "Numerical evaluation of equivalence ratio measurement using OH$*$ and CH$*$ chemiluminescence in premixed and non-premixed methane-air flames," Combust. Flame **156**, 273–291 (2009).
[69] P. Therkelsen, J. Portillo, D. Littlejohn, S. Martin, and R. Cheng, "Self-induced unstable behaviors of CH_4 and H_2/CH_4 flames in a model combustor with a low-swirl injector," Combust. Flame **160**, 307–321 (2013).